Appl. Phys. B 81, 729–752 (2005)
DOI: 10.1007/s00340-005-1989-9

Applied Physics B
Lasers and Optics

Invited paper

E. SOERGEL

Visualization of ferroelectric domains in bulk single crystals

Institute of Physics, University of Bonn, Wegelerstr. 8, 53115 Bonn, Germany

Received: 23 August 2005
Published online: 5 October 2005 • © Springer-Verlag 2005

ABSTRACT In recent years ferroelectric domain patterning has become a popular topic of physical research because it enables photonic applications as well as data storage. For generation of tailored domain structures and for further understanding of ferroelectricity, a visualization of the domain patterns is required. A large number of imaging techniques have therefore been developed. This review summarizes these techniques and highlights systematically their strengths and weaknesses.

PACS 77.84.-s; 78.20.-e; 68.37.-d

1 Introduction

Ferroelectricity was discovered in 1921 by J. Valasek during an investigation of the anomalous dielectric properties of Rochelle salt, $NaKC_4H_4O_6 \cdot 4H_2O$ [1]. It took 14 years until the second ferroelectric material, potassium dihydrogen phosphate (KH_2PO_4, KDP), was found together with some isomorphic crystals [2]. The third major substance, barium titanate ($BaTiO_3$), was reported by A. von Hippel in the 1940s [3]. Since then, this small group of ferroelectric materials has been extended to ~ 250 pure materials and many more mixed crystal systems. Nowadays, ferroelectric materials are intensively investigated because there is still some lack of basic understanding of ferroelectricity although research has been going on for almost fifty years, and because applications that need an optimization of these materials have become important.

A challenging question concerns the minimum size of ferroelectric domains, i.e. down to which size can ferroelectricity still be observed. Experiments with lead zirconate titanate (PZT) nanograins presume a lowest limit of 20 nm by measuring the piezoelectric properties of these grains [4]. Indeed, in experiments with ultra-thin films of bulk lithium tantalate ($LiTaO_3$), domains with a diameter of only 6 nm have been written [5]. It is noteworthy, however, that these two situations cannot be directly compared since (i) the materials are different and (ii) in one case the ferroelectric nanoparticle is not in contact with any material surroundings whereas in the other case it is surrounded by antiparallel polarized material. A directly related topic concerns the width of domain boundaries. While in principle they are atomically sharp, they are known, however, to influence the material through stress and strain even up to several µm away from the domain wall. The growth and manipulation of domains is currently intensively investigated [6] and, related to this, the pinning of domain boundaries at defects is also of interest [7]. Lastly, an as yet unresolved problem in ferroelectricity is the magnitude of the coercive field. The value itself and the reason for large differences in the coercive field with small changes in stoichiometry needs to be clarified [8]. Understanding the origin of an internal electrical field present after domain inversion is also the subject of many investigations [9].

The applications of ferroelectric domain patterning range from optical frequency conversion to high density data storage devices. For the former topic, periodically poled crystals are used and frequency conversion is realized via quasi-phase matching. Although theoretically proposed as early as in the 1960s [10], it took thirty years until periodic poling of $LiNbO_3$ became possible and hence made quasi-phase matching popular [11]. For efficient frequency conversion the dimensions of periodically poled $LiNbO_3$ (PPLN) structures should have an overall length of several cm with a periodicity smaller than $\Lambda = 20\,\mu m$. As an example, to convert IR light of 1064 nm to green light of 532 nm a period length of $\Lambda = 6.8\,\mu m$ is required. For the generation of UV light even smaller period lengths are required. Whereas crystals with large period length can be fabricated through electric field poling, this technique fails for smaller domain widths ($< 1\,\mu m$). To overcome this limitation other mechanisms such as light-induced domain reversal are currently under investigation [12].

Ultra-high-density data storage devices based on ferroelectric domain reversal is another topic which is currently intensively investigated. Ferroelectric random access memory (FRAM) is becoming increasingly commercially relevant, mainly because of its unlimited number of read/write cycles. About ten years ago, a $0.3\,Tbit/in^2$ storage density was shown in thin films of PZT [13]. Today, the storage density has reached $1.5\,Tbit/in^2$ writing domains with a diameter of less than 10 nm in ultra-thin samples of $LiTaO_3$ [5]. For this application, the minimum domain size, and therefore the width of the domain boundaries, is of major importance.

✉ Fax: 0228-73 4038, E-mail: soergel@physik.uni-bonn.de

Further applications concern ferroelectric domain patterning of nonlinear photonic crystals [14], electro-optically controlled diffractive-optical elements such as, for example, electro-optical beam deflectors [15], and electrically controlled Fresnel zone plates [16].

For a better understanding of ferroelectricity and for the control of the written domain structures, it is clear that the visualization of ferroelectric domains is essential. The demand for reliable domain imaging can be estimated from the large number of detection mechanisms reported during the past fifty years. Depending on the particular requirements like image size, lateral resolution, dimensionality of imaging, and temporal resolution, a range of different detection mechanisms has been developed. In this review, the most important techniques for the visualization of ferroelectric domains are presented and discussed.

2 Ferroelectricity

In this section, a brief overview is given of the physical properties of ferroelectric crystals related to the visualization of domains. The second part summarizes relevant fundamental properties of some representative single crystals in which ferroelectric domain imaging is currently intensively investigated, because they play an important role for applications. A table finally provides important parameters of the crystals treated in this review. A detailed description of the physical properties of ferroelectric crystals can be found in Nye [17]. For an overview of the material properties of ferroelectrics and their applications, the book by Lines and Glass has become a standard [18].

2.1 *Properties of ferroelectric crystals*

2.1.1 Ferroelectricity. A crystal is ferroelectric if it has a spontaneous polarization P_s which can be reversed by the application of an electric field larger than the coercive field E_c. Crystalline properties, such as stoichiometry, defect distribution, and conductivity, together with temperature, pressure, as well as electrode conditions, affect the ferroelectric reversal process, and therefore the experimentally determined value of E_c. Reversal or reorientation of P_s is always the result of atomic displacements. All ferroelectric crystals are necessarily both pyroelectric and piezoelectric. They lose these polar properties at the transition (or Curie) temperature T_C.

As a consequence of the spontaneous polarization, the crystal faces perpendicular to the polarization vector carry permanent surface charges, their polarity depending on the orientation of the polarization vector. Based on this surface charging, several methods for domain imaging have been realized.

2.1.2 Piezoelectricity. If stress is applied to certain crystals they develop an electric dipole moment, whose magnitude is directly proportional to the applied stress. This is known as the direct piezoelectric effect. It was discovered by the brothers Pierre and Jacques Curie in 1880 [19]. The word is derived from the Greek piezein, which means to squeeze or press. Each component of the polarization P_i can thus be written as

$$P_i = d_{ijk}\sigma_{jk},$$

with σ_{jk} denoting the stress tensor elements and d_{ijk} the piezoelectric moduli.

The opposite effect exists as well: applying an electric field to piezoelectric crystals results in thickness changes. This is known as the converse piezoelectric effect:

$$\varepsilon_{jk} = d_{ijk}E_i,$$

where the components E_i denote the electric field within the crystal and ε_{jk} denotes the strain tensor.

A variety of methods for domain imaging, especially scanning probe microscopy techniques, rely on the converse piezoelectric effect, whereby a thickness change is measured because of the application of an electric field.

2.1.3 Linear electro-optic effect. The electro-optic effect denotes the fact that an applied electric field alters the refractive index of a crystal [17]. The sign of the refractive-index change depends on the relative orientation of the externally applied electric field and the spontaneous polarization. This can be observed in all-optical investigations as differences in birefringence, phase shift, or reflectivity.

2.2 *Ferroelectric domains*

A region with the spontaneous polarization P_s pointing in one direction is called a ferroelectric domain. As-grown crystals usually have a multi-domain structure, whose relative orientation depends on the crystal symmetry. The majority of ferroelectric crystals exhibits only antiparallel (180°) domains, but also perpendicular (90°) domains can occur (namely in barium titanate ($BaTiO_3$), potassium niobate ($KNbO_3$), or potassium dihydrogen phosphate (KH_2PO_4)). In order to fabricate a single-domain crystal, an external field has to be applied to the crystal during the growth process or during the cooling process to impose a subsequent direction of polarization. Nowadays, several single-domain ferroelectric crystals are commercially available.

2.2.1 Fabrication of ferroelectric domain patterns. Reversing the polarity of a ferroelectric domain requires the application of an electric field along the axis of polarization that exceeds the value of the coercive field E_c. Such electric field poling is currently regarded as the standard technique [20]. In brief, the crystal is electrically contacted with structured electrodes and a voltage ramp or a voltage pulse is used to reverse the orientation of the spontaneous polarization in those areas where the applied electric field exceeds E_c. Structuring of the electrodes is most often realized by lithographic techniques. With this method, regular structures on a large scale (some cm) can be fabricated. The minimum size of the domains, however, is limited to about 3 μm because of domain spreading [21]. In certain crystals, domain inversion can also be reached via indiffusion of titanium through the $+z$ surface near the Curie temperature [22].

Domain patterning in the nm-size regime has been achieved by scanning probe microscopy (SPM), using the tip as an electrode [23–25]. Because the tip radius is of the order of ≤ 30 nm, domain structures in the nm regime in ultra-thin

crystals become possible [5]. Because SPM writing of domain patterns is a sequential technique it is not appropriate for fabricating regular structures on a macroscopic scale (∼ cm). Further techniques are electron-beam writing [26, 27] or light-induced poling [12, 28, 29].

2.3 *Common ferroelectric single crystals*

In this section, a brief introduction is given to those single crystals where ferroelectric domain imaging is frequently needed. It is not a complete list; however, most techniques of ferroelectric domain imaging have been shown at least for one of these materials. Whereas for $LiNbO_3$, $LiTaO_3$, $BaTiO_3$, and strontium–barium niobate (SBN) mixed crystals, several applications have been carried out, and therefore domain imaging is of major importance for improvement of the required domain structures, triglycine sulphate (TGS) and guanidinium aluminium sulphate hexahydrate (GASH) are presented here because they are widely used for investigations of the domain contrast. Table 1 at the end of this section summarizes some important parameters of the crystals treated in this review.

2.3.1 Lithium niobate: $LiNbO_3$. Lithium niobate is one of the most important ferroelectric materials for nonlinear optics, although the first electric field structuring of ferroelectric domains was not realized before 1993 due to the challenge in overcoming the high coercive field of ∼ 20 kV/mm in congruently melting $LiNbO_3$ without damaging the crystal [18, 20, 30]. $LiNbO_3$ belongs to the 3m crystal class with its optical axis, the crystallographic c axis, along the z direction. Ferroelectric domains in $LiNbO_3$ can only occur in the antiparallel 180° configuration along the z direction. Domain boundaries usually follow the crystallographic axes and preferentially form hexagonal domain shapes which penetrate through the whole crystal. Recently, however, surface domain structures of some μm depth with arbitrarily shaped domain patterns have been fabricated [31] and also circular domains which transform to hexagons as they extend into the crystalline z direction have been observed [32].

Because $LiNbO_3$ is not only ferroelectric but also photorefractive and electro-optic, it has a wide range of possible applications and therefore still generates substantial interest for further tailoring and optimization. Varying the stoichiometry or doping, i.e. with iron, are common procedures for extending the range of useful applications [33]. The physical properties of these modified crystals may vary considerably from those of the nominally undoped congruently melting composition.

2.3.2 Lithium tantalate: $LiTaO_3$. Although $LiTaO_3$ is isomorphic to $LiNbO_3$, the niobium being replaced by tantalum, there is a striking difference in the domain formation of these two materials: whereas in $LiNbO_3$ the domains always tend to grow in hexagons, the domain shape in congruently melting $LiTaO_3$ is typically triangular at room temperature and hexagonal above 125°C. Moreover, stoichiometric $LiTaO_3$ generally exhibits hexagonal domain shapes at room temperature, whereas above 200°C they are circularly shaped [34, 35]. As for $LiNbO_3$, only antiparallel 180° domains occur in $LiTaO_3$.

2.3.3 Barium titanate: $BaTiO_3$. As the standard example for a tetragonal perovskite structure, $BaTiO_3$ has been intensively investigated. At room temperature, $BaTiO_3$ exhibits 180° domains which can orient along the six possible directions ($\pm x$, $\pm y$, $\pm z$). This results in configurations where the domain walls are perpendicular to each other, so-called a domains (90°). Therefore, c and a domains can occur on a $BaTiO_3$ surface. Typical domain shapes in $BaTiO_3$ are stripes and rectangles along the right-angled crystallographic axes.

2.3.4 Strontium–barium niobate mixed crystals: SBN. This tungsten-bronze-type crystal is grown in a variety of compositions: $Sr_xBa_{1-x}Nb_2O_6$ with $0.25 < x < 0.75$, where the value of x will severely affect the linear and nonlinear optical coefficients [36]. The standard composition is $x = 0.61$. The material is a relaxor ferroelectric. While SBN was used long ago as a fast pyroelectric detector material [37], nowadays SBN crystals are of interest for optical applications due to their high electro-optic and relatively high nonlinear-optic coefficients. Because SBN is also photorefractive and has

	P_s [μC/cm^2]	$E_c \times 10^5$ [V/m]	Domain configuration	T_C [°C]	Crystal class at room temperature	Domain shape	$d \times 10^{-12}$ [m/V]	References
$LiNbO_3$	70	210	180°	1210	3m	Hexagon	$d_{15} = 70$; $d_{22} = 20$ $d_{31} = -1$; $d_{33} = 6$	[47–49]
$LiTaO_3$	50	210	180°	675	3m	Triangle	$d_{15} = 26.4$; $d_{22} = 7.5$ $d_{31} = -3$; $d_{33} = 5.7$	[48, 50]
$BaTiO_3$	26	0.65	180°; 90°	120	4mm	Stripes	$d_{15} = 329$ $d_{31} = -33$; $d_{33} = 90$	[51–53]
SBN[a]	25	< 5	180°	70	P4bm	Stripes	$d_{33} = 200$	[37, 39, 53, 54]
KTP[b]	20	25	180°	900	mm2	Stripes	$d_{33} = 15$	[55–58]
KDP[c]	5	0.16	180°; 90°	123	$\overline{4}$2m	Stripes	$d_{36} = 23.5$	[58–60]
TGS[d]	2.8	< 10	180°	49	2	Lenticular	$d_{22} = 20$	[18, 61]
GASH	0.35	1.5	180°	–	P31m	Arbitrary	$d_{33} = 2$	[44, 45, 62]

[a] $Sr_xBa_{1-x}Nb_2O_6$ with $x = 0.61$
[b] $KTiOPO_4$
[c] KH_2PO_4
[d] $(NH_2CH_2COOH)_3 \cdot H_2SO_4$

TABLE 1 Some important parameters of selected ferroelectric crystals. Note that the values account for congruently melting, undoped single crystals. P_s: spontaneous polarization, E_c: coercive field, T_C: Curie temperature, d_{ij}: some relevant piezoelectric constants

a low coercive field, a periodic domain pattern can be written into the crystal using the space-charge field generated by two interfering laser beams ('electrical fixing' of holograms [38]). This enables elegant applications such as tunable quasi-phase-matched second-harmonic generation [39]. Ferroelectric domains in SBN are always antiparallel, and their shape is mostly rectangular.

2.3.5 Triglycine sulphate: TGS. Despite its complex chemical and crystallographic form, $(NH_2CH_2COOH)_3 \cdot H_2SO_4$ is frequently investigated because it is one of the few ferroelectrics known to exhibit a second-order phase transition [40]. Below the Curie temperature, TGS exhibits antiparallel 180° domains, along the *b* axis. The shape of the ferroelectric domains in TGS is known to be lenticular or lamellar, elongated along the *a* axis. In addition, TGS is suitable for the study of ferroelectric domain structures and domain dynamics, because it can be cleaved along the *a–c* plane resulting in nearly perfect surfaces perpendicular to the direction of spontaneous polarization [41]. Therefore, TGS is an ideal sample for the investigation of ferroelectric domains by scanning probe microscopy.

2.3.6 Guanidinium aluminium sulphate hexahydrate: GASH. In the 1950s a new class of ferroelectric materials, $C(NH_2)_3Al(SO_4)_2 \cdot 6H_2O$, was discovered [42] and, ten years later, the structure was extensively investigated [43]. GASH exhibits no Curie temperature since it decomposes at $\sim 200\,°C$ before its ferroelectricity is lost. Compared to other ferroelectrics, GASH has an extremely small spontaneous polarization and low coercive field [44]. Furthermore, GASH easily cleaves along the *a–b* plane, perpendicular to the orientation of the antiparallel 180° domains. These properties make the material suitable for direct writing of domain patterns with SPM techniques [45, 46] and for investigations of the contrast mechanism with scanning probe microscopy.

3 Domain detection by surface modifications

As a consequence of ferroelectricity, the surfaces of the crystals perpendicular to the polarization vector are charged. Depending on the crystal material and the circumstances, the surface polarization charge is expected to be under-compensated, just compensated, or over-compensated [63, 64]. However, the remaining electrostatic field at the surface is generally strong enough to allow detection schemes based on charge interaction between the crystal surface and charged or polar particles. Several methods of surface decoration have been developed, but, since the handling is awkward, these techniques are of minor importance nowadays. They will be briefly presented in the following subsection.

Another method that uses modifications of the surface to reveal the ferroelectric domain structures is differential or selective etching. This destructive technique satisfies the standard requirements for the lateral resolution and does not need any special equipment, which may explain why it is the most frequently adopted method for revealing domain patterns. With the appropriate etchant, it can be applied to almost all single crystals. This method is also presented in this section in more detail.

It is self-evident that all surface-modifying techniques only give two-dimensional information of the domain structure at the very surface, and an internal view into the bulk material, i.e. a full three-dimensional imaging of the domain configuration, is not possible.

3.1 *Decoration*

Decoration of the surface has been used as one of the first methods to visualize ferroelectric domain patterns. This technique is based on the spontaneous polarization in the crystal and on uncompensated charges at the surfaces, with their polarity depending on the orientation of the domains. Charged particles such as powders or polar substances (e.g. liquid crystals), but also dew droplets, have been used to reveal the domain configuration.

3.1.1 Powder/Toner. One possible method for domain-selective decoration consists of immersing the crystal in a colloidal suspension of sulfur (yellow) and lead oxide (Pb_3O_4, red) in insulating organic liquids. This produces powder patterns on the faces of the ferroelectric domains [65]. Sulfur in hexane deposits on the negative dipole ends while lead oxide deposits on the positive dipole ends. When using toner for decoration, depending on the solvent and the toner used, it preferentially decorates either the domain boundaries or the negative or the positive domain faces [40, 66, 67]. After evaporation of the solvent the resulting decoration can be imaged photographically. Figure 1 shows an example for toner decoration on a TGS plate.

Although this method is simple to use and has successfully been applied to a variety of crystals such as $LiNbO_3$, $BaTiO_3$, TGS, GASH, Rochelle salt, and glycine sulfate [40, 65], it has never become of great importance. This is mainly because the lateral resolution is low and the handling of the powder-decorated crystals is delicate.

3.1.2 Liquid crystals. Another decoration method for revealing the domain structures uses nematic liquid crystals which orient along the spontaneous polarization at the crystal surface and which can be imaged with a polarizing microscope (Fig. 2) [67].

For orientation, the molecules are squeezed between the crystal and a glass plate. The molecules then align with their long axis parallel to the surface because of mechanical constraint due to the glass plate, and orient because of the electric field which is due to the spontaneous polarization. This

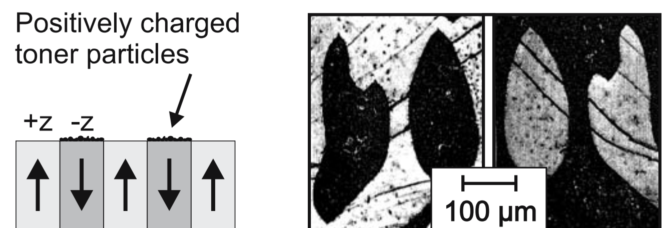

FIGURE 1 Schematics of toner decoration on ferroelectric crystals. As an example, toner patterns on the top and bottom of a TGS plate are shown. Positively charged black toner particles are collected at the $-z$ faces of the ferroelectric 180° domain structures (from Ref. [66])

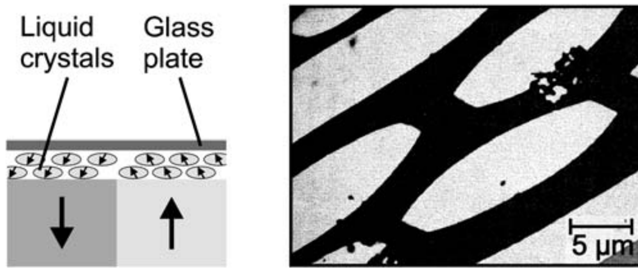

FIGURE 2 With the help of a glass plate, the molecules are spread on top of the crystal. Because they are affected by the spontaneous polarization, they undergo reorientation in correspondence with the domain structures. For observation, a polarizing microscope is used. Example of domains visualized with the liquid-crystal method for a triglycine selenate (TGSe) plate revealing lens-shaped domains with the apex cut (from Ref. [68])

method allows for an in situ observation of the evolution of the domain structure during ageing or temperature variation. As the rearrangement takes time, only slow processes can be imaged. The lateral resolution, as has been demonstrated on a TGS sample, is of the order of 1 μm [68]. This method was further developed, and investigations showed that domain structures in non-polar cuts (i.e. 180° domains that lie in the plane of the surface) could also be imaged [68–70]. However, as this technique needs freshly cleaved or cleaned, polished surfaces that are not yet polluted by the adsorption of impurities and neutralized by other charges, it has never achieved wide application.

Although this method has not become a standard for imaging ferroelectric domain structures, it has conversely been used for local alignment of nematic liquid crystal molecules. Therefore, small areas of a $BaTiO_3$ thin film have been poled with a scanning force microscope and immersed within the nematic liquid crystals to be aligned [71].

3.1.3 Dew. For curiosity, a further method of domain imaging is briefly presented here: dew as surface decoration (Fig. 3) [72]. The experimental procedure is as follows: the crystal is placed in a closed chamber, at a temperature slightly below that of the vapor to be condensed. Sucking vapor (e.g. isobutyl alcohol) into the chamber gives a condensation pattern on the crystal surface. At the domain boundaries large drops form, whereas on the faces of the domains only small droplets are visible. The whole setup is placed below an optical microscope in order to observe the dew pattern. Images have to be taken within a few seconds, before the droplets evaporate again. The drops have diameters of 0.5 to 2.5 μm,

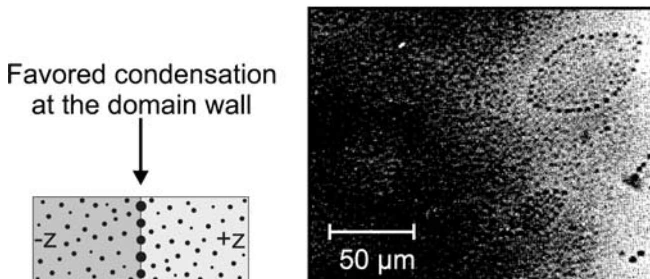

FIGURE 3 Lenticular domains in a TGS crystal made visible by the dew method using the vapor of isobutyl alcohol (from Ref. [72])

which is sufficient to reveal domain structures of 5-μm size on a TGS sample.

The reason for the preferential collection of drops at the domain boundaries might lie in the strong field gradient at this region, therefore attracting smaller droplets nearby. This technique is qualitatively similar to that used in cloud chambers invented by C.T.R. Wilson about one hundred years ago to visualize the traces of charged particles as droplets in a supersaturated gas mixture. Although the lateral resolution for domain imaging is high, because of the relatively complicated experimental procedure this method has never become widespread.

3.2 *Etching*

The most common, although destructive, method for the visualization of ferroelectric domains is selective etching, also named differential etching. The method is based on the different etch rates for the positive and negative ends of ferroelectric dipoles. A schematic of the selective etching process is shown in Fig. 4.

For observation of the resulting etch patterns, there are three main possibilities: (a) a direct observation with an optical microscope, and to achieve higher lateral resolution (b) imaging of the etched structures with a scanning electron microscope or (c) topographic imaging with a scanning force microscope (Fig. 5).

Differential etching was first used in $BaTiO_3$ to reveal antiparallel 180° ferroelectric *c* domains [73]. It has been shown that the etch rate for the positive titanium end of the dipole is much faster than for the negative oxygen end. For domains with the polarization direction parallel to the crystal surface (*a* domains), the etch rate was found to be intermediate between the rapid $+z$ and the slow $-z$ rates. As an etchant, hydrofluoric acid (HF) [74, 75], H_3PO_4 [76], and hydrochlo-

FIGURE 4 Selective etching for the visualization of antiparallel ferroelectric domains in z-cut $LiNbO_3$, where the $-z$ face etches much faster in hydrofluoric acid (HF) than the $+z$ face, for which the etch rate is unmeasurably small

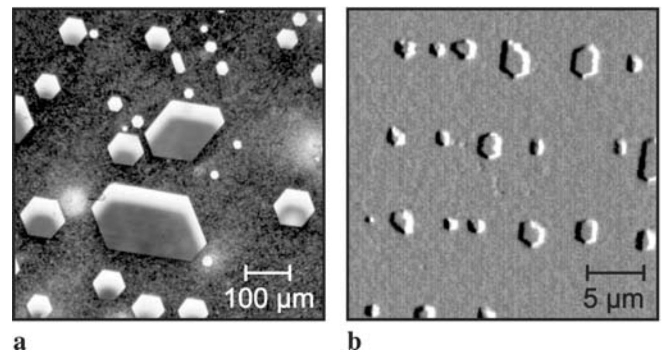

FIGURE 5 Two examples of images of $LiNbO_3$ crystals etched in hydrofluoric acid. (**a**) As seen with an optical microscope (from Ref. [83]), (**b**) the topography detected by scanning force microscopy (from Ref. [12])

ric acid (HCl) [73] were used which all preferentially etch the $+z$ faces of the domains.

A decade later, the first results for etching of antiparallel domains in $LiNbO_3$ were reported [77]. It has been observed that for this material, the etch rate at the negative $-z$ face is much faster than the one at the positive $+z$ face. In this first paper, a multi-domain crystal was etched in a mixture of one part of hydrofluoric acid (HF) and two parts of nitric acid (HNO_3) at the boiling point ($\approx 110\,°C$): after 10 min a clear distinction of the domain structure was attained. Nowadays, some fourty years later, the etching properties of $LiNbO_3$ are still an active field of research: the influence of different dopants [78], the dependence on the stoichiometry [79] and temperature [80], as well as the choice of the right etchant [81] and the theoretical understanding of the etching process [82] are still under investigation.

Etching of $LiTaO_3$ was found to be very similar to the case of $LiNbO_3$. Also, mainly the $-z$ face is attacked by the pure HF or mixtures of HF and HNO_3 [84, 85]. In SBN, it was found, however, that the $+z$ face etches faster than the $-z$ face when using a 37% solution of HCl at room temperature [86]. In KTP (potassium titanyl phosphate, $KTiOPO_4$) the $-z$ face is attacked in a KOH : KNO_3 solution [87], and also TGS [88, 89] and GASH [90] can be selectively etched to reveal the domain structure.

Etching is primarily applied because it is acknowledged to be a strong indication for the existence of ferroelectric domains. Furthermore, it is fast, relatively simple, and has a resolution $< 0.1\,\mu m$. The attainable lateral resolution is limited by the so-called sidewall etching, where the non-polar crystal faces are also attacked, which becomes important with increasing etching times [78, 91, 92]. However, etching has two main drawbacks: (i) it is a destructive method, i.e. at least the top 50 nm of the crystal are affected and (ii) it therefore does not permit in situ imaging of domain-reversal processes.

Although etching was originally developed for the detection of ferroelectric domain patterns, it has since become an important tool for microstructuring ferroelectric materials. Single tips for scanning probe applications [93] and ridge waveguides [80] have been fabricated, and even free-standing cantilevers have been made [81]. Surface-relief gratings have also been realized by this microstructuring method [94, 95].

3.3 *Comparative summary: surface-modifying techniques*

For comparison of the different techniques, Table 2 shows a summary of their main features. As they all reflect the properties of the surface, three-dimensional imaging of the domains is not possible. Also, because of a lack of lateral resolution, the real width of the domain boundary is not accessible by these methods.

From all the techniques presented in this section, differential etching is most frequently used. It is generally recognized to definitively show domain structures, i.e. successful selective etching is a very strong argument for the existence of a domain pattern.

4 Domain detection by optical methods

In this section, all-optical methods to visualize ferroelectric domains or domain boundaries are presented, excluding point-by-point scanning procedures that will be addressed in Sects. 5 and 6.

Optical methods have the advantage of being non-contact and non-invasive, and usually they allow a real-time observation of the domain-formation process. Furthermore, some of the detection schemes enable a depth-resolved analysis of the domain configuration in the bulk material. However, the diffraction-limited lateral resolution of about $1\,\mu m$ is a serious drawback. There are attempts to overcome this limitation with, for example, scanning confocal microscopy and scanning near-field microscopy (Sects. 5 and 6).

Optical intensity contrast of ferroelectric domains via homogeneous illumination of the sample with light of wavelengths ranging from X-rays to the near infrared can be accounted for due to phase-front distortion resulting from the dependence of the refractive index on the orientation of the optical c axis or from the photorefractive effect. Other methods have employed second-harmonic generation or simple imaging of the topography that is altered by the presence of antiparallel domains. Experimental setups using these contrast mechanisms will be discussed in this section.

The most versatile physical property that is useful to optically visualize ferroelectric domains relies on refractive-index changes induced by the linear electro-optic effect. Indeed, depending on the experimental setup used, either the domain faces or the domain boundaries can be visualized. In the case of antiparallel 180° domains, the crystal needs to be strained to cause different refractive indices between the $+c$ and the $-c$ domains which can be accomplished, for example, by applying an electric field along the optical axis [96]. A transparent crystal holder with liquid electrodes can effectively be utilized for this, as is shown in Fig. 6. The crystal is mounted with O-rings between two glass plates and contacted via water electrodes, for example to apply an electric field along the c axis. Some crystals such as $LiNbO_3$ and $LiTaO_3$ exhibit long-lived internal fields following inversion of the domains that

Method	Lateral resolution	Real time	Shown for
Powder/Toner	$1\,\mu m$	–	$LiNbO_3$, $BaTiO_3$, TGS, GASH
Liquid crystals	$1\,\mu m$	Slow	TGS, TGSe, GASH, KTP
Dew	$2\,\mu m$	–	TGS
Differential etching	$0.1\,\mu m$	–	$LiNbO_3$, $LiTaO_3$, $BaTiO_3$, SBN, TGS, GASH, KTP

TABLE 2 Comparison of the surface-modifying techniques for the visualization of ferroelectric domain patterns. The lateral resolution has been estimated from images shown in Sect. 3 or extracted from the references given in the text

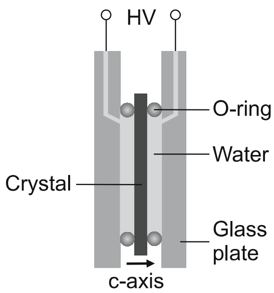

FIGURE 6 Crystal holder for the observation of ferroelectric domains with simultaneous application of an electric field. HV denotes the high-voltage source. This setup can be used to reverse domains applying a high voltage while simultaneously observing the poling process in real time

persist for as long as the crystals have not been annealed [97, 98]. These internal fields themselves can be sufficient to observe the antiparallel domain structures without the need for applying any additional external field.

4.1 *Polarization microscopy*

Investigations of ferroelectric domains with polarization microscopy started over sixty years ago imaging *a* and *c* domains in KH_2PO_4 (KDP) [99]. Some years later, domain structures in $BaTiO_3$ were also probed with this method [100]. To see the domain structures, the sample has to be put between crossed polarizers. Because of the different refractive indices of *a* and *c* domains, a retardation occurs leading to a contrast in the observed image. The technique is fast and simple, and is therefore still a favored method for a preliminary visualization of ferroelectric domains. For $BaTiO_3$, one has to distinguish among three types of domain boundaries [96, 101]:

- *a* domains parallel and *c* domains perpendicular to the observed surface. This results in black *a* faces and bright *c* faces.
- *a* domains perpendicular to each other, but both in the plane of the observed surface. The domain boundaries appear as black lines, and the orientation of the domains can be determined by the rotation of one of the polarizers.
- Antiparallel *c* domains perpendicular to the surface. They can only be optically revealed when the crystal is strained or by illuminating it with oblique light [75].

A very early photograph of domain structures in a $BaTiO_3$ crystal is shown in Fig. 7. From images in a recent publication the lateral resolution can be estimated to be of the order of some μm [102].

Indeed, for crystals exhibiting only antiparallel 180° domains, an electric field to cause strain has to be applied for the visualization of the domain patterns through polarization microscopy. The interpretation of the resulting images, however, is evident.

Polarization microscopy has also been combined with near-field scanning optical microscopy, thereby overcoming the limited lateral resolution [7]. This will be further discussed in Sect. 6.2. Furthermore, polarization microscopy also reveals the birefringence at the domain boundaries due to stress of freshly poled domains. This can be used for the in situ observation of the poling process in $LiNbO_3$ and in $LiTaO_3$ [34, 103].

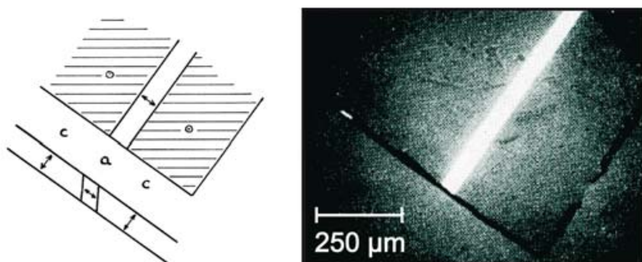

FIGURE 7 Polarization microscopy: schematic sketch and photograph of a 90° *a* domain between two *c* domains in $BaTiO_3$ (from Ref. [101])

4.2 *Light deflection*

A promising new technique for the observation of domain patterns relies on the phenomenon of light deflection at the domain boundaries [104]. This method is especially suited for monitoring domain reversal in real time for applications such as fast and easy estimation of the quality of PPLN crystals [105].

For investigation, the sample is mounted in a quartz-glass holder (for transparency in the UV, similar to that shown in Fig. 6), electrically contacted with transparent liquid electrodes (water) and illuminated with an unexpanded ultraviolet or blue laser beam, along the crystallographic *c* axis. By applying a voltage to the crystal along the *c* axis, the laser beam undergoes deflection at the domain boundaries, and the resulting light pattern can be viewed on a screen. The setup is schematically depicted in Fig. 8.

The physical mechanism behind this visually dramatic experiment is depicted in Fig. 9. An incident plane wave is partially deflected at the domain boundaries through an angle α given by

$$\alpha = |2\Delta n d/D| = |n_0^3 r_{13} E_{\text{ext}} d/D|,$$

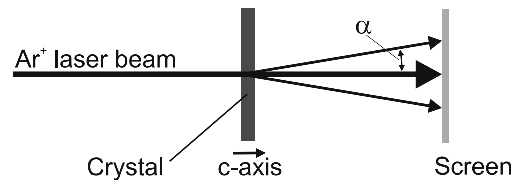

FIGURE 8 Setup for the investigation of ferroelectric domain boundaries via light deflection in the far field (α: deflection angle). The crystal holder is shown in Fig. 6

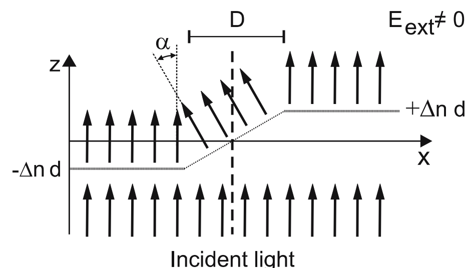

FIGURE 9 Light deflection at a domain boundary under the influence of an external field E_{ext}. Due to the electro-optic effect an external field leads to opposite refractive-index changes Δn in antiparallel domains. Here d denotes the crystal thickness, and D the width along which the phase front is continuously changing. Part of the wave is therefore deflected by the angle α [83]

where n_0 denotes the initial ordinary refractive index, r_{13} the appropriate electro-optic coefficient [104], and d the crystal thickness. From the measured result of $\alpha = 8°$ the width D of the discontinuity was estimated to be about 15 μm. This was also sustained by measuring the ratio of the deflected and transmitted light as well as by a wavelength-dependent study of the diffraction broadening of the affected beam [83]. It is worth noting that D has nothing to do with the domain width but results directly from diffraction broadening of the phase front of the beam as it transits the sample.

In the case of $LiNbO_3$ with an arbitrary domain structure, the light pattern, as observed in the far field, shows a six-pointed star, because the domains are mainly hexagons (Fig. 10a). The same experimental setup can, of course, be utilized for the investigation of $LiTaO_3$ crystals [106]. However, here the preferred domain shapes are triangles, and therefore the far-field image shows a three-pointed star. The direction of the rays with respect to the domain boundaries depends on the polarity of the applied electric field (Fig. 10b). Although this visualization technique has up to now only been applied to $LiNbO_3$ and $LiTaO_3$, there is no reason why it should not be applied to other single crystals.

In the case of PPLN structures the domain pattern acts as a refractive-index grating giving rise to several discrete, equally spaced diffraction maxima and minima [105]. Analyzing these patterns allows a quality control of the PPLN sample with respect to duty cycle, period length, and homogeneity.

It is worth noting that the investigation of domain patterns by laser-beam deflection as described above gives information on large crystal areas, integrating over all domains within the laser beam (diameter typically 2 mm). Therefore, no detailed spatially resolved conclusions can be derived from such essentially averaging measurements.

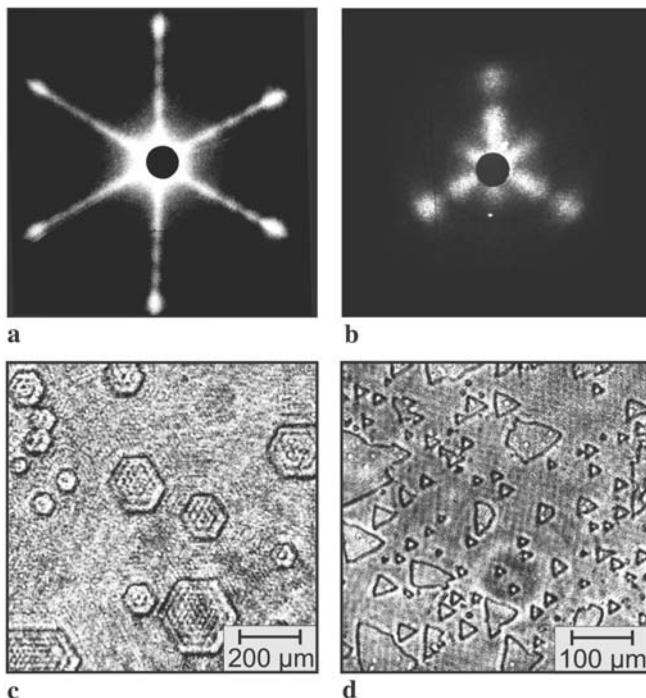

FIGURE 10 The *upper row* shows the deflected light patterns in the far field and the *lower row* the corresponding domain structures imaged in the near field (Sect. 4.3) for $LiNbO_3$ (**a**) and (**c**), and $LiTaO_3$ (**b**) and (**d**) (from Ref. [104])

4.3 *Near-field method*

A simple optical technique, which yields laterally resolved images of ferroelectric domain boundaries, is the visualization of the light distribution in the near field. Figure 11 shows the simplified experimental setup, which is identical to the one shown in Fig. 8 (Sect. 4.2) except that in addition a focusing lens is introduced that images the back side of the crystal. The laser beam illuminates the crystal along the c axis and experiences a phase shift that gives rise to an interference pattern between the light waves on both sides of a domain boundary [104]. Applying the appropriate voltage one can maximize the phase shift and therefore the contrast in the near-field image.

Images of near-field light patterns of $LiNbO_3$ and $LiTaO_3$ crystals with domain structures are shown in Fig. 10c and d together with the corresponding far-field images of the deflected light beam. The near-field method is extremely useful to monitor domain reversal in real time with a lateral resolution of about 10 μm, as can be estimated from Fig. 10d.

4.4 *Interference and birefringence*

A further all-optical method for domain imaging is based on the detection of the interference pattern of a linearly polarized laser beam that is reflected at the front and at the back faces of the crystal. A schematic drawing of the setup is shown in Fig. 12 with the polarizer P oriented in transmission with respect to the incoming laser beam. Light being reflected at the back face travels back and forth through the crystal and experiences a phase shift depending on the orientation of the domains and the voltage applied: the different phase shifts cause a phase jump in the interference pattern which can be recorded with a CCD camera.

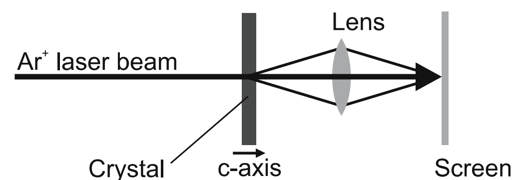

FIGURE 11 Setup for the investigation of ferroelectric domain boundaries via light deflection in the near field. The crystal is placed in a holder as shown in Fig. 6

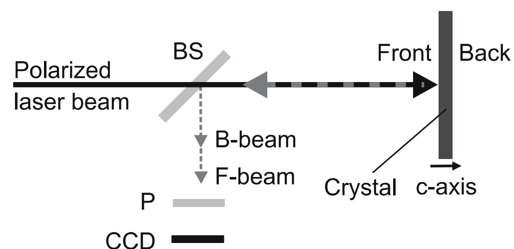

FIGURE 12 Setup for the investigation of ferroelectric domain boundaries via interference and electro-optic phase changes. Here F-beam (B-beam) denotes the laser beam reflected at the front (back) face of the crystal. The crystal is placed in a holder as shown in Fig. 6

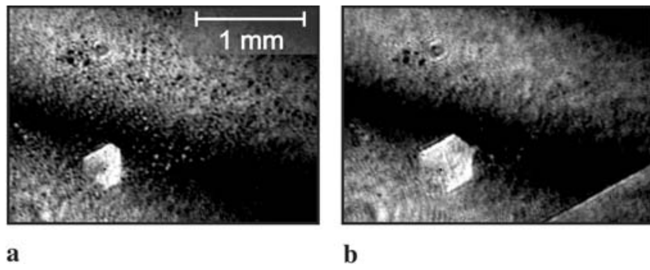

FIGURE 13 In situ visualization of domain growth in a Mg : $LiNbO_3$ crystal in the presence of an increasing external electric field. In (**a**) only a single domain is present which has grown in (**b**), and in addition from the *lower right corner* a domain wall enters the image (from Ref. [107])

The setup shown in Fig. 12 can also be used to visualize the additional birefringence at the domain walls, now with the polarizer oriented perpendicular to the polarization of the incoming laser beam. Only light from the back face of the crystal can experience a change in polarization which occurs at the domain boundaries because of stress, and therefore they appear as bright lines on the CCD camera.

It is also possible to combine the two methods presented above, setting the polarizer to an intermediate angle, whereby the contribution of the two detection mechanisms can be adjusted by choosing the appropriate angle of the polarizer (Fig. 13).

4.5 *Photorefractive grating method*

Imaging ferroelectric domains using a photorefractive grating is based on the fact that the phase of holographically written refractive-index gratings with respect to the light interference pattern depends on the orientation of the ferroelectric domains [108]. A simplified drawing of the experimental setup is shown in Fig. 14.

To reveal the domain configuration a refractive-index grating is written in the crystal via the photorefractive effect [109, 110]. Because the linear electro-optic coefficients differ in sign for antiparallel ferroelectric domains, the corresponding refractive-index gratings are shifted by a phase of π with respect to each other. This is only true, however, if diffusion and drift of the charge carriers are the dominating charge-driving forces because they are independent of the domain orientation. By comparing the light interference pattern (that was used to write the grating) with the read-out light intensity pattern (generated by illuminating the crystal with a single laser beam) the domain configuration in the crystal can be determined by imaging the light distribution at the exit face of the crystal with a microscope objective onto a CCD camera. A proof of principle has been carried out with Ce:SBN crystals [108]. As this method relies on the Bragg selectivity of a thick grating, however, it is only suitable for thick crystals. The spatial resolution is limited to several microns not because of the resolution of the microscope, but mainly due to the diffraction mechanism itself, since only deviations from periodicity extending over several grating periods can be detected.

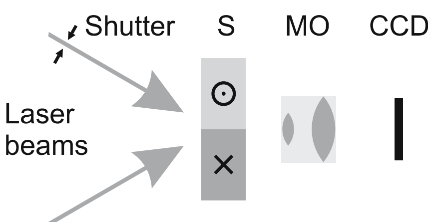

FIGURE 14 Principle of domain visualization via the photorefractive effect. Two interfering laser beams overlap inside the sample (S). For read out one of the laser beams is blocked by a shutter, and the back side of the sample is imaged with a microscope objective (MO) onto a CCD camera

Besides the poor lateral resolution, the main drawback of this method is the restriction to photorefractive crystals whose charge-transport mechanism does not rely on the bulk photovoltaic effect [111, 112], therefore excluding the most frequently used ferroelectric crystals, namely $LiNbO_3$ and $LiTaO_3$.

4.6 *Photorefractive beam-coupling method*

Another technique involving the photorefractive properties of the crystals uses two-beam coupling. Here the intersecting laser beams, which generate the photorefractive grating, enter the crystal from different faces: the probe beam is aligned exactly along the optical *c* axis and the pump beam is almost orthogonal to it (Fig. 15) [113].

The direction of the *c* axis determines the sign of the two-beam coupling gain, i.e. the probe beam either gains or loses intensity depending on the orientation of the domains.

This method can be extended to a three-dimensional mapping of the domain patterns, therefore also revealing domain structures hidden inside the crystal. For this purpose, the pump

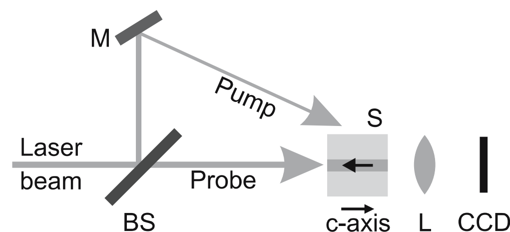

FIGURE 15 Setup for beam coupling in a $BaTiO_3$ crystal. A probe beam travels exactly along the *c* axis of the crystal and takes energy away from a pump beam by photorefractive two-beam coupling, except in crystal regions containing 180° domains. Any 180° domain hidden in the crystal appears as a dark spot on the CCD camera (BS: beam splitter, M: mirror, S: sample, L: lens)

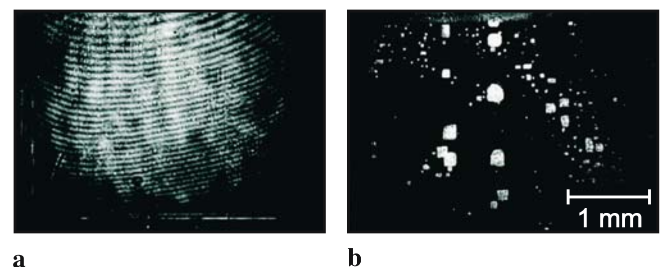

FIGURE 16 Profile of the transmitted signal beam (**a**) with the pump beam absent and (**b**) with the pump beam switched on. Each *bright square* corresponds to a 180° domain. The fringes in (**a**) are due to interference of beams from the front and the back sides of the crystal. (**b**) shows one of 20 data slices, all orthogonal to the *c* axis, used to construct a three-dimensional map of the domains inside the crystal (from Ref. [114])

beam is collimated with a cylindrical lens, illuminating only a small slice of the crystal which is successively translated in steps along its *c* axis [114]. The transmitted signal beam is shown in Fig. 16: with the pump beam absent (a) and with the pump beam switched on (b), showing such a data slice. This technique allows a real three-dimensional reconstruction of domain structures hidden in $BaTiO_3$ crystals with a lateral resolution of ∼ μm, given by the resolution of the CCD camera and restricted by the width of the illuminated slice.

4.7 *Second harmonic generation microscopy (SHGM)*

Although second-harmonic generation (SHG) is mainly used for generating short-wavelength laser light via frequency doubling, it can also be applied to directly observe domain configurations. It was first reported for TGS single crystals more than 30 years ago [115], but is still an actual visualization technique, mainly applied to periodically poled domain structures [116]. A very much simplified setup is depicted in Fig. 17.

By illuminating a uniform SHG plate with a Nd:YAG laser beam ($\lambda_1 = 1064$ nm) part of the light is converted to $\lambda_2 = 532$ nm. In the crystal to be investigated, light of wavelength λ_2 is also generated. Since in the case of 180° domains the sign of the second-order nonlinear coefficients is opposite for neighboring domains and the generated light of wavelength λ_2 is out of phase by π, respectively, the domain structure can be visualized through interference with the light generated by the uniform SHG plate. An example of this technique showing the inspection of a PPLN crystal is presented in Fig. 18a. 90° domain structures in $BaTiO_3$ can also be observed in a similar setup, because of the difference in amplitudes of the second-order nonlinear coefficients [117].

Other schemes use SHG to visualize the domain boundaries of single crystals [118]. The SHG enhancement observed in the domain walls can be ascribed to the effect of field enhancement and depolarization near small scatterers. For observation, the uniform SHG plate (Fig. 17) is omitted and the

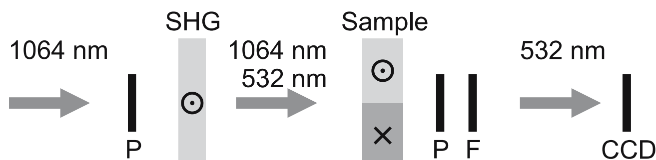

FIGURE 17 Optical setup for the second harmonic generation microscope. SHG: uniform second harmonic plate, P: polarizer, F: infrared absorption filter, CCD: camera

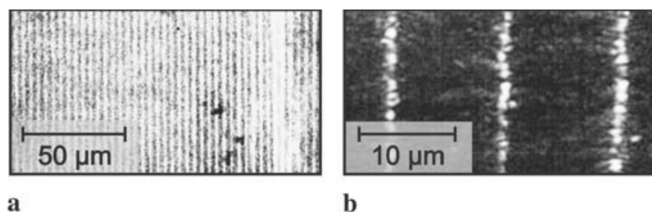

FIGURE 18 (**a**) Image of a PPLN crystal (period length 3.8 μm, depth of the domains ∼ 2 μm) showing the domain faces (from Ref. [116]) by second-harmonic generation. (**b**) Image of a PPLN crystal (period length 20 μm, bulk domains) showing the domain boundaries via light scattering (from Ref. [118])

domain walls are observed directly (Fig. 18b). Three-dimensional images providing a high lateral resolution (∼ 2 μm) can also be obtained by SHG imaging [119]. Another setup images periodically poled structures via the far field of the non-phase-matched SHG light pattern: if the domain boundaries are tilted relative to the input and output faces of the crystal, the far-field second-harmonic light consists of multiple beams, in contrast to the single beam generated in a single-domain crystal. From the angular separation of these beams one obtains a measure of the tilt of the domain walls if the refractive-index difference $n_{2\omega} - n_{\omega}$ is known [120].

In order to obtain high lateral resolution, the technique of second-harmonic generation has also been applied to the detection of ferroelectric domains with scanning confocal microscopy (Sect. 5.4) [121] and with scanning near-field microscopy (Sect. 6.3) [122].

4.8 *X-ray imaging*

First experiments analyzing ferroelectric domains in single $NaNO_2$ crystals by white X-ray Laue diffraction were conducted over forty years ago [123]. Since that time, high-resolution X-ray diffraction imaging (also known as high-resolution chromatic X-ray topography) has become an important tool for the visualization of ferroelectric domains. Using a synchrotron X-ray source, the crystals can be investigated using large-area beams with high brightness. This allows measurements in transmission (Laue geometry) and in reflection (Bragg geometry) in 1-mm-thick crystals with high lateral resolution of about 1 μm, as has been shown for SBN and $BaTiO_3$ [124]. The domain visibility is explained via dynamical diffraction [125], an effect which depends on the lack of inversion symmetry in the unit cell.

Another detection scheme for X-ray imaging takes advantage of the highly coherent beams from third-generation synchrotron sources: periodically poled samples exhibit a phase shift between adjacent domains. Different explanations for this phenomenon have been given: lattice distortions changing the direction of propagation of a wave diffracted from the crystal [126] or a phase shift between the structure factors of the adjacent domains [127]. This technique allowed the imaging of ferroelectric domains of a PPLN crystal and also of a periodically poled $KTiOAsO_4$ (KTA) crystal [128]. The

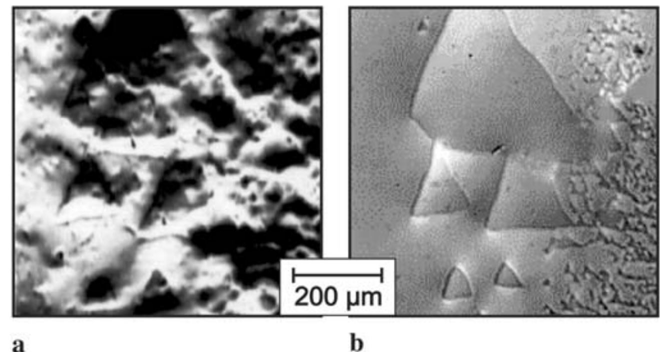

FIGURE 19 (**a**) Antiparallel 180° domains in congruent *z*-cut $LiTaO_3$ crystals visualized using an 8 keV X-ray Bragg-diffraction image (**a**). For comparison (**b**) shows the same area imaged by optical microscopy (from Ref. [130])

lateral resolution is about 10 μm, as can be estimated from images of a study of domains in KTA [87, 129].

A different approach to determine the domain structure via X-ray imaging lies in the detection of the distortion of the Bragg matching due to strain at the domain walls. In a recent paper, X-ray imaging was used to estimate the width of strain associated with 180° domain walls in congruent $LiNbO_3$ and $LiTaO_3$ crystals, which turned out to be of the order of several μm (Fig. 19) [130, 131]. A similar number for the strain width has also been found for 90° domains in $BaTiO_3$ by X-ray microdiffraction [132].

4.9 *Comparative summary: optical techniques*

Table 3 summarizes the different visualization techniques described above. Compared to the other detection methods presented in this review, they have two main advantages: nearly all of them allow a real-time imaging of the domain structure, e.g. during polarization reversal. Secondly, some of them offer the possibility of full three-dimensional imaging of the domain structures, therefore allowing quality control of nominally single domain crystals.

5 Domain detection by scanning microscopy techniques

This section is dedicated to optical and electron microscope techniques in which the image is generated by scanning. Compared to the methods presented in Sect. 4, the image acquisition is not achieved in a single shot but via scanning of the sample on a pixel by pixel basis. Therefore, observing domain formation in real time is in general not possible by scanning techniques, except if the process is very slow (e.g. at low temperatures). However, because of their good lateral resolution these visualization methods are nevertheless an important tool for the investigation of ferroelectric domains.

5.1 *Scanning electron microscopy (SEM)*

Imaging ferroelectric domains with scanning electron microscopy (SEM) is challenging because all ferroelectrics are by nature dielectric materials that are highly insulating [133]. However, by operating the SEM with low acceleration voltage, 180° domain patterns in TGS, $LiNbO_3$, $BaTiO_3$, KTP, and GASH have been observed in the secondary electron emission mode (reflection) [134–136]. There are several possible explanations for the domain contrast. One is based on electrostatic interaction: when the sample is irradiated by the primary electron beam, secondary electrons are emitted from a certain depth below the surface. At the positive end of the dipole, some primary electrons are captured: hence, there is a stronger secondary emission and therefore a brighter contrast from the negative end [133, 137]. Another possible explanation lies in the converse piezoelectric effect: the sample contracts or expands depending on the domain orientation because of the electric field generated by the electrons deposited at the surface [135]. Also, the pyroelectric effect may play a role, because of the heating of the sample by the electron beam, and this too has been proposed to explain domain contrast [135]. Finally, an asymmetry of elementary electron processes in non-centrosymmetric crystals was suggested [136]. Although the domain-contrast mechanism in SEM imaging is still under discussion, the method can non-destructively visualize domain patterns with submicron resolution [138]. Figure 20 shows the schematic setup and an image taken with the SEM technique.

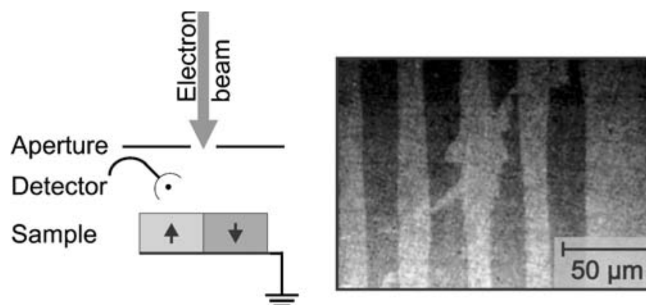

FIGURE 20 Schematic setup for SEM and antiparallel 180° domains in $LiTaO_3$ (from Ref. [138])

SEM has also been used to directly write domain patterns in $LiNbO_3$ single crystals. The writing mechanism can be represented as local-electric-field poling because $LiNbO_3$ is an insulator and hence the charges of the electrons generate an electric field across the crystal, which triggers polarization reversal [26, 27].

5.2 *Scanning electron acoustic microscopy (SEAM)*

Based on a standard scanning electron microscope, scanning electron acoustic microscopy (SEAM) detects the

Method	Lateral resolution	Three-dimensional	Orientation	Real time	Shown for
Polarization microscopy	Some μm	–	90°	√	$BaTiO_3$
			180° (*E*)		All
Light deflection	–	–	180° (*E*)	√	$LiNbO_3$, $LiTaO_3$
Near-field method	10 μm	–	180° (*E*)	√	$LiNbO_3$, $LiTaO_3$
Interference and birefringence	10 μm	–	180° (*E*)	√	$LiNbO_3$, $LiTaO_3$
Photorefractive grating method	Several μm	–	180°	–	Ce:SBN
Photorefractive beam-coupling method	10 μm	√	180°	√	$BaTiO_3$
Second-harmonic generation	1 μm	√	180°	√	TGS, $BaTiO_3$, $LiNbO_3$, KTP
			90°	√	$BaTiO_3$
X-ray imaging	1 μm	–	180°	√	SBN, $BaTiO_3$, $LiNbO_3$, $LiTaO_3$

(*E*) denotes that the application of an externally applied electric field is necessary for visualization

TABLE 3 Comparison of the optical methods for domain detection. The lateral resolution was estimated from images similar to the ones shown above or extracted from the references given in the text

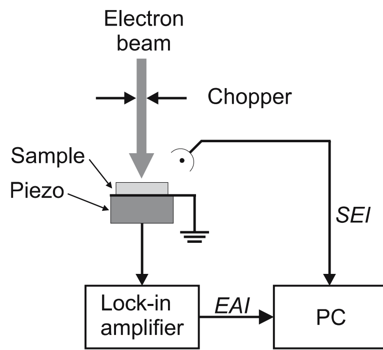

FIGURE 21 Schematic setup of scanning electron acoustic microscopy. An electron beam is focused on the sample, and the acoustic waves generated due to the converse piezoelectric effect are detected as an electric signal with a piezoelectric transducer. For better signal-to-noise ratio the electron beam is chopped, and read out is performed with a lock-in amplifier. The electron acoustic image (EAI) or the SEAM image carries information about the domain configuration. The secondary electron image (SEI) depicts the topography of the sample

piezoelectric response of the sample [139]. Figure 21 shows the experimental setup: an intensity modulated focused electron beam hits the sample leading to a local charge distribution at the surface. A modulated electric field builds up, which, due to the converse piezoelectric effect, expands or contracts the sample with respect to the orientation of the domains, thereby generating acoustic waves. For read out, the sample is mechanically contacted to a piezoelectric transducer, and the resulting electrical signals are detected with a lock-in amplifier. The phase of the signal yields the orientation of the domains. Simultaneously to this so-called electron acoustic image (EAI) carrying information about the domain structure of the sample, the backscattered electrons can be recorded leading to a secondary electron image (SEI) showing the surface topography of the sample, as explained in the previous paragraph. Figure 22 shows an example for a periodically poled $BaTiO_3$ crystal.

SEAM has been applied to the investigation of ferroelectric $BaTiO_3$ single crystals [139], ceramics [140], and PPLN [141]. Although the experimental setup is completely different, the principle of domain imaging is the same as in scanning near-field acoustic microscopy (Sect. 6.4).

5.3 *Transmission electron microscopy (TEM)*

Because it requires extremely thin samples, visualization of ferroelectric domains in transmission electron microscopy (TEM) is usually adopted for the investigation of ferroelectric ceramics [142–147]. The first detailed study of ferroelectric domain boundaries in $BaTiO_3$ with holographic imaging TEM was performed about twenty years ago [148]. Although these investigations were carried out imaging a single grain in a powder sample, TEM also works for single crystals as long as they permit the transmission of the electron beam for imaging. From the published figures, the lateral resolution of this method can be estimated to be < 10 nm. The extension to HRTEM (high-resolution TEM) is an attempt at quantitative measurement of the thickness of ferroelectric domain walls in $BaTiO_3$ [149], which has been measured to be < 2 nm.

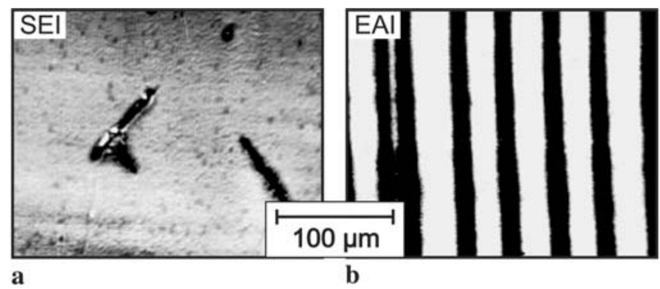

FIGURE 22 Images of a $BaTiO_3$ single crystal with SEAM. The secondary electron image (SEI) depicts the topography of the sample (**a**). The electron acoustic image (EAI) or the SEAM image (**b**) carries information about the domain configuration (from Ref. [139])

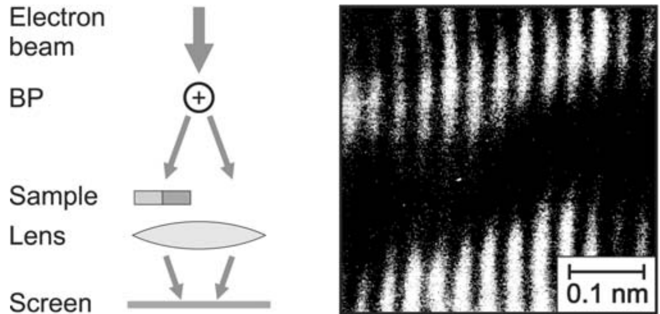

FIGURE 23 Schematic setup for the electron holographic visualization of ferroelectric domain boundaries, and a hologram showing interference fringe splitting across a 90° domain wall in $BaTiO_3$; BP: electrostatic biprism (from Ref. [153])

In $PbTiO_3$ a similar domain-wall thickness has also been found [150–152].

In another detection scheme, the TEM is used to perform electron holography, employing the original concept of Gabor with two interfering electron beams [154]. Applying this technique to ferroelectric domain boundaries is based on a change of the phase front of the transmitted electron beam that depends on the domain orientation [155]. This technique allows the detection of 90° domains with a high lateral resolution of about 2 nm [153]. For investigation, the crystals have to be polished mechanically and subsequently thinned by ion milling. To generate two interfering electron beams, an electrostatic biprism is placed below the objective lens of the microscope and, by applying an appropriate voltage, fringe spacings of < 0.5 nm can be realized. The resulting holographic interference patterns show a bending or splitting (Fig. 23) of the fringes at the domain boundaries, which leads to an estimate of the width of the domain walls [153].

5.4 *Confocal scanning optical microscopy (CSOM)*

In confocal scanning optical microscopy (CSOM) [156] a diffraction-limited spot of polarized light is scanned across the sample. Visualization of 180° domains with this technique was first demonstrated in thin films of $(Ba, Sr)TiO_3$ ceramics [157]. In further studies, the method was applied to $LiNbO_3$ with PPLN structures [158]. By applying an alternating electric field along the optical axis simultaneously to illumination with a polarized laser spot, the amplitude and/or phase of the reflected light are affected. This modulation of the reflected light depends on the domain orientation, because

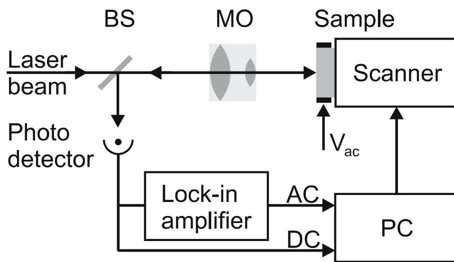

FIGURE 24 Schematic setup for CSOM. A linearly polarized laser beam is focused on the sample to which a modulated voltage V_{ac} is applied along the *c* axis. The reflected light is detected with a lock-in amplifier. The dc signal reveals the topography of the sample, while the ac signal reveals the domain structure. BS: beam splitter, MO: microscope objective

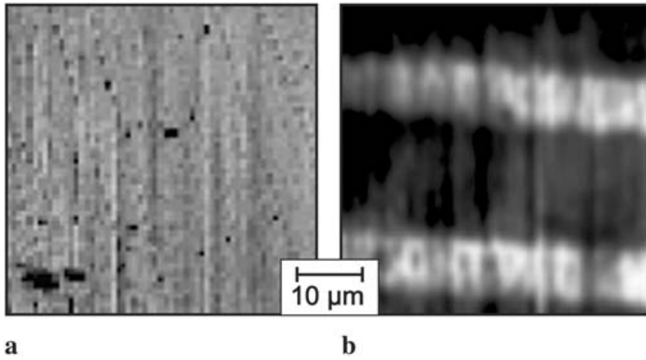

FIGURE 25 Scanning confocal image of a $LiNbO_3$ crystal with a periodically grown domain structure in (**a**) dc mode resolving the topography and (**b**) ac mode showing the domain structure (from Ref. [159])

the sign of the electro-optic effect also depends on the domain orientation. The sign of such changes is opposite for antiparallel domains, and its value depends on the angle between the light polarization plane and the crystal axis [158]. A schematic drawing of the experimental setup is shown in Fig. 24.

The lateral resolution of this method as estimated from the images published is about 1 µm [158]. A useful feature of this technique lies in the possibility of focusing slightly below the surface, therefore reducing influences on the detected image by the surface roughness. A further property of this detection mechanism is the possibility of performing time-resolved measurements by using a pulsed laser and therefore revealing, for example, the growth process of domain structures [159]. Figure 25 shows the topography (a) and the CSOM image (b) for a periodically poled $LiNbO_3$ crystal.

5.5 *Second-harmonic microscopy (SHM)*

This visualization method uses a laser scanning microscope adapted for second-harmonic generation and detection [121]. Even though the lateral resolution is about 1 µm, it has the ability of three-dimensional imaging of the domain structure inside bulk samples, as has been shown for $LiNbO_3$ and $BaTiO_3$ [121, 160]. This detection mechanism provides a contrast only at the domain boundaries, which is explained by the local disturbance of the linear and nonlinear properties of the crystal at the domain walls [160]. Figure 26 shows examples of experimental data obtained with a periodically poled $LiTaO_3$ (PPLT) sample.

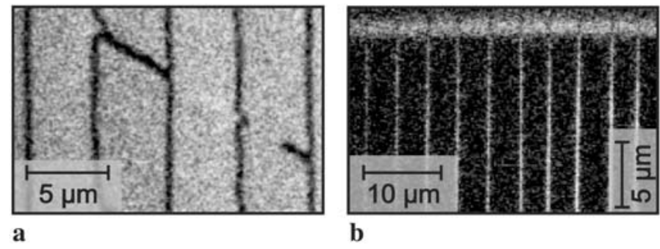

FIGURE 26 Second-harmonic image of a periodically poled $LiTaO_3$ crystal. (**a**) $+z$ face and (**b**) x face of the sample (from Ref. [160])

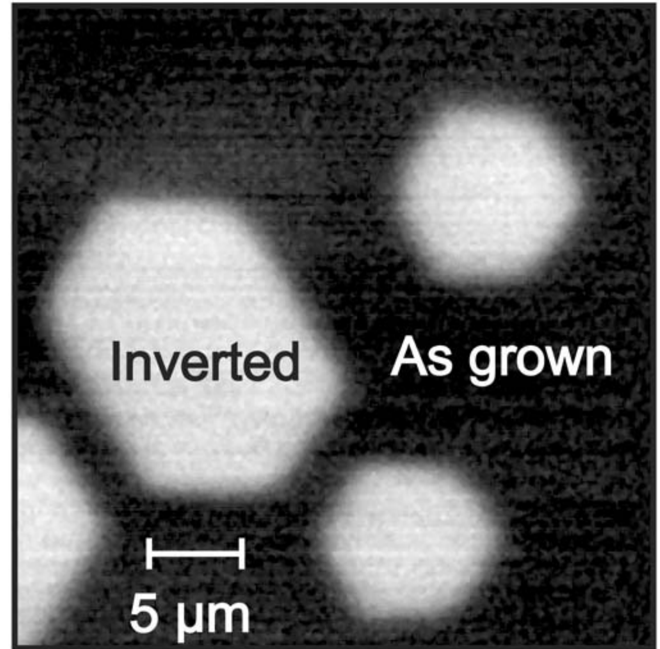

FIGURE 27 Image of domain structures and walls in a congruent Er^{3+}-doped $LiNbO_3$ single crystal measured at room temperature using a confocal luminescence microscope (from Ref. [162], see also Ref. [163])

5.6 *Defect-luminescence microscopy (DLM)*

This method is based on light emission of Er^{3+} ions that were intentionally introduced into the crystal. Domain-inverted regions are distinguishable because the spectral properties of Er^{+} depend on the poling state. Using site-selective excitation-emission spectroscopy, a contrast in the domain orientation can therefore be imaged and, by introducing the detection method into a confocal luminescence microscope, ferroelectric domain structures can be measured with a spatial resolution of about 700 nm [161]. Furthermore, this method offers a temporal resolution of 50 ms for a single pixel, which makes it ideally suited to study real-time dynamics of domain walls. The physical reason for the contrast lies in a rearrangement of the defect complexes during the domain inversion [162]. Figure 27 shows a DLM image of domain structures in a $LiNbO_3$ crystal.

It is worth noting that with the same setup domains in bulk $LiNbO_3$ could be written directly with feature sizes of about 2 µm [29]. In addition to the focused laser spot, an electric field 25% below the regular coercive field was applied to the sample.

Method	Lateral resolution	Three-dimensional	Shown for
SEM [a]	< 1 µm	–	$LiNbO_3$, $LiTaO_3$, $BaTiO_3$, TGS, GASH, KDP
SEAM [b]	10 µm	–	$LiNbO_3$, $BaTiO_3$
TEM [c] – HRTEM [d]	1 nm	–	$BaTiO_3$, $PbTiO_3$
TEM – holographic	2 nm	–	$BaTiO_3$
CSOM [e]	1 µm	–	$LiNbO_3$
SHM [f]	1 µm	√	$LiNbO_3$,$LiTaO_3$, $BaTiO_3$
DLM [g]	< 1 µm	–	Er : $LiNbO_3$

[a] scanning electron microscopy
[b] scanning electron acoustic microscopy
[c] transmission electron microscopy
[d] high-resolution transmission electron microscopy
[e] confocal scanning optical microscopy
[f] second-harmonic microscopy
[g] defect-luminescence microscopy

TABLE 4 Comparison of the scanning microscope techniques for domain detection. The lateral resolution was estimated from images similar to the ones shown above or extracted from the references given in the text

5.7 *Comparative summary: scanning microscopy techniques*

Table 4 summarizes the key features of the methods presented in this section.

6 Domain detection by scanning probe microscopy techniques

6.1 *Scanning force microscopy (SFM)*

In an early paper, only some years after the first realization of a scanning force microscope (SFM) [164], this imaging technique was applied to measure antiparallel 180° ferroelectric domains in $Gd_2(MoO_4)_3$ (GMO) [165]. It was the beginning of a broader activity of scanning force microscopy applied to the detection of ferroelectric domains. Other scanning probe microscopes (SPMs) developed since this first report, predominantly near-field scanning optical microscopes, were also successfully used to image domain patterns and to better understand domain formation and dynamics. Although several microscope types and modes of operation from the large variety of SPMs have been applied to the investigation of ferroelectric domains, the SFM is still the most used instrument. The interpretation of the measurements, however, is still challenging because of the physical complexity of ferroelectrics and the large number of possible interactions between tip and sample. This is also indicated by the large number of publications dealing in general with the contrast mechanism of ferroelectric domain imaging with scanning force microscopy (see e.g. Refs. [63, 166–170]).

A key point in the discussion is whether the origin of ferroelectric domain imaging by SFM (in contact mode with a modulated voltage applied to the tip) is based on the converse piezoelectric effect, as primarily suggested, which measures a thickness change of the sample by applying a voltage via the tip [45, 46, 171, 172], or whether other physical properties of ferroelectric domains are responsible for the image contrast, such as for example the polarization charge density [61, 173, 174], different work functions of adjacent domains [175], or also other tip–surface interaction schemes [63, 169] (to name a few examples only). The main objective of these investigations is to clarify the contrast mechanism and thereby to find an answer to the following question: if there is a contrast, does it unambiguously prove the existence of domains?

6.1.1 Operation modes of the scanning force microscope relevant to ferroelectric domain imaging. In this section, a brief overview of the different modes of operation of a SFM is given to better categorize the investigations presented later. Detailed descriptions of SFM techniques can be found elsewhere [176, 177]. For a rough classification of the different SFM techniques the feedback mechanism is selected as indicated below:

– Contact mode: repulsive force regime, the tip is in permanent contact with the surface. The feedback loop ensures a constant bending of the cantilever.
– Non-contact mode: attractive force regime, the tip–surface distance is 1–10 nm. For operation, the cantilever is mechanically driven to oscillate at its resonance frequency (oscillation amplitude ∼ 2 nm), and the feedback loop adjusts the tip-to-sample distance to maintain, for example, a constant oscillation amplitude.
– Lift mode^{TM} [178]: measurements in this mode are performed in two successive steps: firstly, a line is scanned in contact or non-contact mode to determine the topography. Then, on the way back, the tip is lifted to a predetermined height, typically 50 to 100 nm above the surface, and scanned over the previously measured topography.

The SFM operation modes itemized above can be employed for insulating or conducting and electrically contacted cantilevers. In the latter case, one can choose to ground the tip, to apply a dc voltage, or to apply an ac voltage (with an optional dc offset). Note that it makes no difference whether the voltage is applied to the tip and the electrode at the back side of the sample is grounded or vice versa. Because the end of the tip is very sharp ($r \approx 10$ nm), the field at the tip can reach values up to 10^8 V/m for an applied voltage of only 10 V [46]. However, the field is much weaker even a very short distance below the tip inside the sample: it can be seen from simple

considerations that depending on the tip radius r and the dielectric constant ε of the sample, the field drops to $\ll 10\%$ of its initial value within 1-μm depth. This was experimentally confirmed by the measurement of domain structures that change their shape within a depth of 10 μm along the z axis of a $LiNbO_3$ crystal [32].

A further general point relevant for the interpretation and understanding of ferroelectric domain imaging with SFM is the influence of the cantilever–sample interaction. From simple size considerations (cantilever width × length is about 30 μm × 200 μm) and from the achievable lateral resolution in SFM measurements (better than 50 nm), it becomes clear that the influence of the cantilever–sample interaction cannot play a dominant role, unless the sizes of the domains are comparable to that of the cantilever. In this case, for cantilevers with weak spring constants this interaction could account for blurred phase images [179].

One more general feature of SFM imaging should be pointed out: although the SFM is sensitive to subatomic features [180], this resolution can only be reached by making a serious experimental effort for the setup and recording small images ($\ll 1 \times 1\ \mu m^2$). A standard commercial SFM has a lateral resolution comparable to the tip radius (≈ 10 nm) and a vertical resolution of ≤ 0.1 nm for images of about $50 \times 50\ \mu m^2$ with an acquisition time of some 10 min. These numbers just give a rough idea of the resolution limits usually achievable with standard SFM measurements.

In the following, the different detection schemes that have been applied to the investigation of ferroelectric domains are discussed separately according to the classification described above.

6.1.2 Contact mode with insulating tip. A series of experiments using insulating Si_3N_4 tips on GASH and TGS single crystals were reported [62, 181]. For GASH, the 180° domain faces appeared to have reversed contrast. The imaging process was attributed to charge trapping by the tip as it scans the surface causing an electrostatic interaction between the statically charged tip and the surface polarization charges. For TGS the reported domain shape was not lenticular, as expected from other visualization techniques [134]. Although irregularly shaped domain walls may exist for temperatures close to the Curie temperature, they may easily be confused with surface topographic features. For TGS, the interpretation of the recorded images is even more delicate because ambient humidity already selectively etches the surface. The abovementioned experiments could not be satisfactorily explained and much discussion ensued (see also Ref. [16] in [182] and Ref. [24] in [183]).

If the tip is in contact with the sample, frictional forces arise that can also be detected as a torsion signal of the cantilever. Also, for this detection method, investigations of GASH and TGS have been performed [182, 183]. On GASH, the forward and the backward scans showed an inverted domain contrast. This was explained by the structural differences between the surfaces of oppositely polarized domains which modify the surface potential experienced by the tip, resulting in two different friction coefficients (Fig. 28a). Electrostatic interactions between tip and sample were excluded from having a significant influence on the measured lateral force [182]. In other experiments investigating TGS surfaces with friction force, the expected lenticular domains could be imaged – the shape itself being a strong argument that domains are actually being detected (Fig. 28b) [182, 183]. Earlier experiments were probably influenced by topographic artifacts and therefore did not clearly resolve the domains [62]. The contrast in friction force for TGS was ascribed to different chemical compositions of the surfaces of oppositely polarized domains and to asymmetric surface potentials [182].

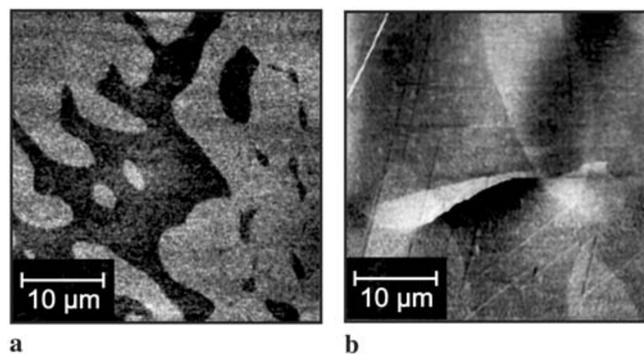

FIGURE 28 Friction force microscopy images on a GASH surface (**a**) interpreted as irregularly shaped domain structures (from Ref. [182]) and on a TGS surface (**b**) showing lenticular domain shapes (from Ref. [183])

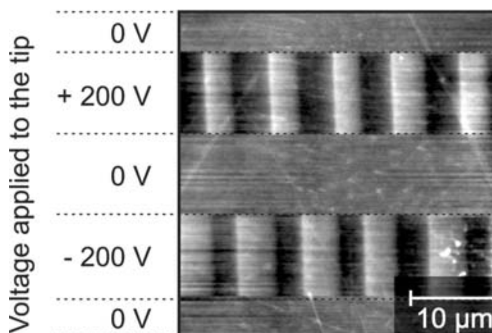

FIGURE 29 Topographic image of a PPLN structure recorded in contact mode with a dc voltage applied to the tip. During image acquisition, the applied voltage was varied between −200 V, 0 V (tip grounded), and +200 V (from Ref. [184])

6.1.3 Contact mode with conducting tip: V_{dc} applied. This detection scheme directly provides information on the piezoelectric response of the sample because the thickness change (i.e. shrinkage or expansion) depends on the orientation of the domains. Indeed, scanning the z face of a PPLN sample with an applied voltage of $V = 200$ V, the theoretically expected thickness change of $\Delta h = V d_{33} d = 1.5$ nm, where $d = 0.5$ mm is the thickness of the crystal and $d_{33} = 7.5 \times 10^{-12}$ m/V is the appropriate piezoelectric coefficient for $LiNbO_3$, has been measured [184]. The measured thickness change scales linearly with the applied voltage and can be reversed by changing the sign of the voltage (Fig. 29). Also, scanning the y face, contrast resulting from the piezoelectric coefficient d_{22} could be confirmed. Similar experiments have also been carried out with RTP ($RbTiOPO_4$) crystals [185].

Noteworthy, however, is that although at the very tip the electric field might be as high as 10^8 V/m, this has no influence on the amplitude of the piezoelectric response of the

sample, as shown in Ref. [186]. This is because as long as the material responds linearly, the field distribution has no relevance for the measured thickness change of the material; the applied voltage, i.e. the integrated field, is the only relevant parameter for the deformation. However, mechanical constraints, because of the small volume of the deformation, might have an effect. Estimations of the piezoelectric deformation, calculated with the high electric field at the tip as if it were applied throughout the whole thickness of the sample, are therefore not valid and result in expected values for the thickness change which are too large by several orders of magnitude (see e.g. Ref. [45]).

6.1.4 Contact mode with conducting tip: V_{ac} applied. This is by far the most used SFM-based detection scheme. In the literature, two names are used for this method: (i) dynamic-contact electrostatic force microscopy (DC-EFM), which therefore only describes the operation mode, with no indication of the possible contrast mechanism and (ii) piezoelectric or piezoresponse force microscopy (PFM), suggesting that the piezoelectric effect (in whatever manner such as mechanical deformation or electrical charging) is responsible for what is detected. Unfortunately, the term PFM is also employed if only a part of the measured tip–sample interaction can be attributed to the piezoelectric response. Regardless of this, in the following, PFM will be used only if the image contrast is expected to be dominated by piezoelectric contributions.

Because of the importance of this detection mechanism, the setup is depicted schematically in Fig. 30. The conducting tip is electrically contacted, and a modulated voltage V_{ac} with an optional offset voltage V_{dc} is applied. V_{ac} typically has an amplitude of 5–15 V and a frequency of 5–50 kHz. The feedback in contact mode is slow and hence not affected by the periodically modulated movement of the cantilever. Read out of the DC-EFM (or PFM) domain signal is performed with a lock-in amplifier, measuring the amplitude of the cantilever vibration and its phase with respect to the applied modulated voltage.

Imaging antiparallel 180° ferroelectric domain structures with PFM, i.e. measuring the expansion or contraction of the sample caused by the converse piezoelectric effect, has to satisfy two basic preconditions: the detected signals between antiparallel 180° domains must be (i) of equal amplitudes and (ii) have a π phase shift between them. At the domain boundary the amplitude is reduced because of mechanical constraints. Figure 31 shows such a measurement on a $LiNbO_3$ single crystal [187]. Note that in the case of ferroelectric thin films (ceramics) these features might not be fulfilled because of the inhomogeneity of the sample within the depth probed by the tip [188]. However, for bulk materials these two general requirements for PFM contrast in ferroelectric domain imaging are also not generally fulfilled: to achieve a π phase shift the 'right' choice of the voltage modulation frequency seems crucial [35, 172], a phenomenon that indicates additional contributions to the oscillating signal from the cantilever.

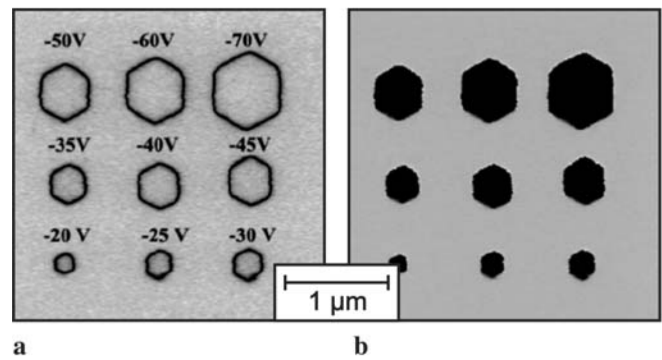

FIGURE 31 Domains written in stoichiometric $LiNbO_3$ with voltage pulses of 10-ms duration and different magnitudes. (**a**) shows the amplitude of the PFM image and (**b**) the phase (from Ref. [187])

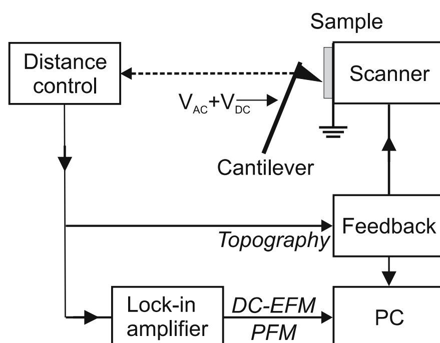

FIGURE 30 Schematic setup for the DC-EFM or PFM operation mode of SFM. An alternating voltage V_{ac} (with an optional offset V_{dc}) is applied to the conducting tip. The back side of the sample is grounded. A contact-mode feedback is used. The domain signal is read out with a lock-in amplifier operating at the frequency of the alternating voltage V_{ac} that is applied to the tip

Indeed, the PFM signal should be independent of the frequency of the applied voltage (< 100 kHz) because the electro-mechanical resonance frequency of bulk ferroelectric crystals is very high (in the GHz regime for $LiNbO_3$ and $LiTaO_3$ [189]). However, frequency scans in the kHz range show a complex spectrum, and the amplitude and the phase of the measured domain signal depend clearly on the frequency [166, 172, 190, 191]. In recent experiments, a deeper insight into the frequency behavior as observed for DC-EFM measurements has been obtained [192]. In those experiments it was observed that a very similar frequency spectrum can be detected using a standard glass microscope slide as the sample, which cannot by definition exhibit any piezoelectric response, indicating that the ferroelectric behavior of the sample is not the cause of the observed frequency spectrum.

The spring constant of the cantilever is also known to influence the DC-EFM signal, which is not consistent with the purely piezoelectric explanation for the signal. Weak cantilevers (low resonance frequency) show little or no signal [193], which might result in a blurred phase image as described above [179]. An elaborated, theoretically sustained investigation of the influence of the indentation force of the tip on the sample has also been carried out [169, 194, 195]. Other authors suggest that only stiff cantilevers can follow the movement of the surface [179], thereby allowing the measurement of a 180° phase shift between adjacent domains [35, 172].

Furthermore, if image contrast is achieved by the converse piezoelectric effect, the vibration amplitude of the cantilever has to agree with the theoretical values for the thick-

ness changes deduced from the known piezoelectric constants (see Table 1). The mechanical constraint, because of the adjacent non-vibrating crystal regions and the possibly nonlinear response at the very surface because of the extremely high electric field, has only a small diminishing influence on the signal [184, 186]. A rough estimation yields a piezo-driven thickness change of only 0.1 nm for a voltage of 10 V applied to the tip for a material having a piezoelectric constant of 10×10^{-12} m/V. As explained above, the expected thickness change is independent of the field distribution at the very tip, depending only on the applied voltage. Indeed, some experiments measured thickness changes of up to 30 nm in $LiNbO_3$ [35, 196] and 5 to 30 nm for GASH [45, 46], whereas others claim to having clearly resolved a thickness change of only 0.02 nm in KTP [171], and measurements in GaN of only 1-pm height variation have been reported [188]. However, in most publications no value for the vibration amplitude of the cantilever is reported.

An attempt to resolve some of the difficulties in explaining the experimental results of PFM measurements can be to assume a mechanical excitation of the SFM head through the tip that is in contact with the vibrating surface. This would be helpful for explaining the complex phase and frequency scans, and also the large amplitudes of the signal could be accounted for by resonance properties of the system. Finally, the dependence of the effect on the spring constant (as being the coupling between the sample and the SFM head) would also fit into this scheme. However, it is clear that further investigations must be carried out to make firm conclusions in this case.

Scanning nonlinear dielectric microscopy: SNDM is a further development of contact-mode imaging with an ac voltage applied to the tip [197, 198]. In this detection scheme, the sample is part of a capacitor in an LC resonant circuit. The voltage applied to the tip is modulated in the GHz range. A change of the capacitance, induced by a change in the nonlinear dielectric response of the sample, therefore gives information about the local ferroelectric polarization. This imaging technique achieved an excellent lateral resolution in the sub-nm range [199]; however, the $LiTaO_3$ samples used were only ≈ 100-nm thick [5]. This detection method has also been applied to single $BaTiO_3$ crystals, clearly resolving 90° and 180° domains [200]. This technique was used to investigate a high-density data-storage device (Fig. 32), where writing and detecting ferroelectric domain structures is achieved with the SFM tip [201].

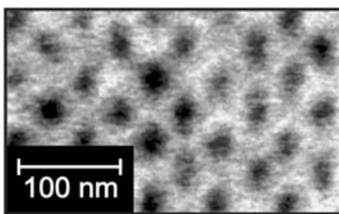

FIGURE 32 Scanning nonlinear dielectric microscopy image of close-packed array of domain dots at a data density of 0.62 Tbit/in^2. The dots were written with voltage pulses of 11 V, 10-ms duration in a 70-nm-thick $LiTaO_3$ single crystal (from Ref. [5])

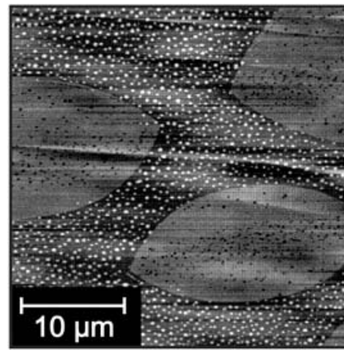

FIGURE 33 Non-contact SFM image of a TGS surface clearly showing the expected lenticular shape of the domains. The direction of spontaneous polarization is perpendicular to the surface (from Ref. [183])

6.1.5 Non-contact mode with insulating tip. This is a very unusual detection scheme because the potential of the tip is, in fact, undefined – image charges (induced by the surface charges) or fixed charges (dust particles, friction charging) are expected to play a major role for domain contrast in the recorded images [62]. The investigations described below were carried out with stiff, insulating Si_3N_4 cantilevers [183]. Experiments on TGS showed a clear lenticular shape of the antiparallel 180° domains as observed with other visualization techniques [133]. Furthermore, an upper limit for the width of the domain wall of 8 nm was claimed, although this cannot be estimated from the image (Fig. 33) [183]. A further proof of the ferroelectric domain nature of the observed structures was performed by heating the sample above its Curie temperature. In this case, the structures disappeared. The image contrast is explained via electrostatic forces acting on the tip. Similar results were found for $BaTiO_3$, revealing 90° domains, also vanishing by heating above the Curie temperature. Unfortunately, no antiparallel domains were found in that sample [183].

6.1.6 Non-contact mode with conducting tip: V_{ac} applied. The detection of electrostatic surface charges with a scanning force microscope (SFM) is usually performed in the non-contact mode, applying a moderate alternating voltage of

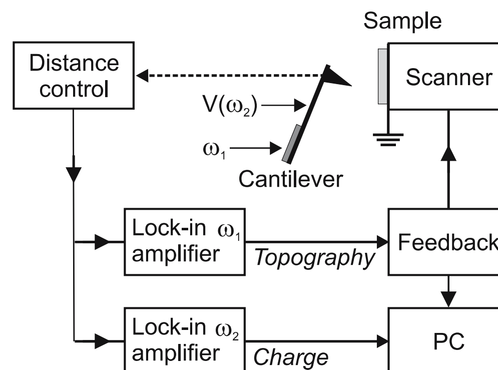

FIGURE 34 Block diagram for the electrostatic force microscope in non-contact mode. The cantilever is mechanically driven at its resonance frequency ω_1 to implement the feedback circuit. For charge detection, an alternating voltage (frequency ω_2) is applied to the tip, and the response of the tip is detected with a lock-in amplifier (at ω_2)

FIGURE 35 Simultaneously recorded topography (**a**) and electrostatic force signal (**b**) of an as-grown SBN crystal with an arbitrary domain structure (*stripes*). The topography shows a crystal step (height 1.2 nm) (from Ref. [205])

some volts to the tip and demodulating the signal with a lock-in amplifier [202, 203]. From the amplitude of the signal, the charge density can be estimated, whereas the phase gives information about the polarity of the charges measured. This detection method was shown to be sensitive enough to measure single elementary surface charges [204]. Figure 34 shows a block diagram of the setup.

Detection of ferroelectric domains with electrostatic force microscopy relies on measuring the charge distribution at the surface, which is due to the polarization of the domains. Depending on the material investigated, the surface charge density may rise to such high values that a stable operation of the SFM in non-contact mode is not possible any more, i.e. the forces between charged tip and surface charges become much stronger than the van der Waals forces used for the feedback control. This is, unfortunately, the case for $LiNbO_3$. For other crystals and ceramics, however, this method may be applied successfully. With this detection method a lateral resolution of better than 100 nm has been attained.

The very first imaging of ferroelectric domains with SFM was achieved with this technique on $Gd_2(MoO_4)_3$, or GMO, detecting antiparallel 180° domains which showed opposite contrast [165]. Investigations of SBN crystals showed the same behavior (Fig. 35) [205]. Also, single crystals of GASH and TGS were investigated with this detection scheme [62, 181]; however, only the domain walls showed a contrast (see also Ref. [206]). This was explained by an induced dipole in the tip due to the electric field from the surface polarization of the domain structures in the sample. The force gradient acting on the dipole is strongest in the inhomogeneous field at the domain boundaries – therefore, they are highlighted in the images.

FIGURE 36 Block diagram of the electrostatic force microscope in lift mode. The topography is recorded during the forward scan (f) and the charge distribution is measured during the backward scan (b) which is accomplished at a predetermined height of 50 to 100 nm above the surface. During the backward scan a voltage V is applied to the tip

FIGURE 37 Lift-mode EFM images. *Left*: titanium indiffused ferroelectric domains in a $LiNbO_3$ crystal: (**a**) a topographic image of the grating, (**b**) the electrostatic force image observed over the same area (from Ref. [208]). *Right*: GASH sample imaged with the dynamic operation mode. A 5-V bias is applied to the tip (from Ref. [209])

6.1.7 Lift mode. Detection of surface charges can also be achieved in the lift mode, probing the surface at a large distance free of any topographic influence [207]. A schematic of the lift mode for detection of ferroelectric domains is shown in Fig. 36. In the forward scan, the topography is determined and, in the backward scan, the tip is lifted to a predetermined height, and a dc voltage is applied to the cantilever. Electrostatic interactions of the charged tip and surface charges result in a bending of the cantilever. With this read-out scheme, the first ever imaging of 180° domains in $LiNbO_3$ by SFM was achieved (Fig. 37) [208]. Also, the domain structure in freshly cleaved GASH surfaces could be detected.

A small variation of this detection scheme is the dynamic operation mode, which is sensitive to the force gradient. During the backward scan, the cantilever is mechanically oscillated close to its resonance frequency. The force gradient which arises from the sample stray field causes a shift of the resonance frequency, which subsequently is determined by measuring the phase lag between the oscillation of the excitation and that of the cantilever itself. In addition, a voltage can be applied to the tip, thereby obtaining information about the polarity of the surface charges.

Furthermore, experiments in the lift mode under a controlled inert-gas atmosphere have been carried out showing that the domain contrast strongly depends on the ambient conditions as well as on the dc voltage applied to the tip [208]. This indicates that the polarization surface charges are at least partly compensated by charged particles of the surrounding gas.

Although this detection mechanism allows a very clean separation of the electrostatic signal, i.e. the domain signal, from topographic artifacts, it is not generally suitable for the investigation of ferroelectric domain structures because the large tip-to-sample distance limits the lateral resolution to about 1 µm.

6.2 *Near-field scanning optical microscopy (NSOM)*

Scanning optical microscopy techniques like CSOM (Sect. 5.4) or DLM (Sect. 5.6) have a diffraction-

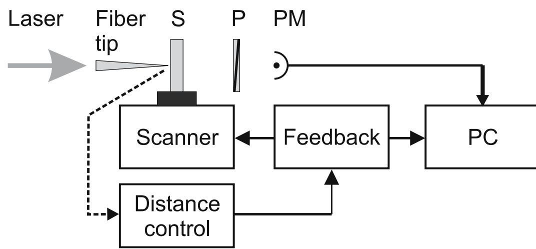

FIGURE 38 Schematic setup of an illumination mode NSOM. Polarized laser light directed through the optical fiber acts as the tip, which has an aperture size of ≈ 50 nm. The light passing through the sample (S) is collected by a photomultiplier (PM) behind an optional polarizer (P). The feedback is achieved with a distance control based on the shear-force method (not explicitly drawn)

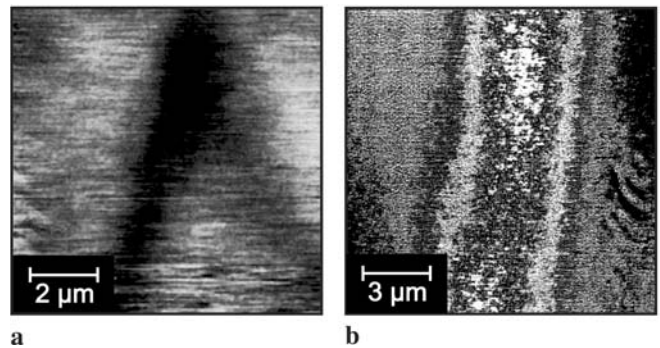

FIGURE 39 NSOM illumination mode image (**a**) of the corner of a triangular domain in $LiTaO_3$ observed due to strain-induced birefringence. NSOM collection mode image (**b**) of a ferroelectric domain boundary in a $LiTaO_3$ crystal with an additional electric field applied to the sample (from Refs. [7, 213])

limited spatial resolution of the order of the wavelength. To overcome this strong limitation, a near-field technique has been developed, the called near-field scanning optical microscope (NSOM) [210, 211]. Usually, a tapered fiber with an aperture size of ≈ 50 nm is used as a tip and the transmitted light is detected with a photomultiplier, determining intensity, phase, and polarization. For NSOM two operation modes are possible: (i) the illumination mode as shown in Fig. 38 (only a small section of the sample is illuminated through the fiber tip) and (ii) the collection mode (only light from a small area of the sample is collected by the fiber tip). The lateral resolution of NSOM images is assumed to be of the order of the size of the aperture. For feedback control, the shear force detection scheme is most common, which enables the tip-to-sample distance to be maintained at a few nm [211, 212].

For the investigation of ferroelectric domain boundaries, an NSOM setup in illumination mode (i) can be used [213, 214]. The samples were partially poled z-cut $LiTaO_3$ single crystals (0.5-mm thick) and illuminated through the fiber tip with a polarized HeNe laser beam (633 nm). The transmitted light was detected with a photomultiplier. The 180° domain walls are visible because of strain-induced birefringence, which persists as long as the crystal is not annealed. The domain walls could be imaged with a lateral resolution of about 200 nm and the regions of increased birefringence were measured to be 1-µm wide.

In collection mode (ii), where the sample is illuminated from the side opposite to the scanning fiber tip, ferroelectric 180° domain walls in $LiNbO_3$ and $LiTaO_3$ could also be imaged due to birefringence with a lateral resolution of ≈ 100 nm [7, 215]. To observe pinning and bowing of domain walls, the surfaces of the samples were covered with 20-nm-thick semitransparent conducting layers and electric fields were applied to the crystals to trigger domain growth. In this detection mode, the additional distance of the tip from the crystal surface, typically 20 nm, however, can affect the lateral resolution. The regions of increased birefringence across a domain boundary were measured to have a width between 100 nm and 3 µm.

Another application of NSOM in collection mode relies on detecting second harmonic generated light with high spatial resolution (Sect. 4.7). It has so far only been applied to the investigation of a piezoceramic PZT sample, and yielded a lateral resolution of about 150 nm illuminating the sample with Nd:YAG laser light at 1064 nm and detecting the generated green light through the fiber tip with a photomultiplier [122].

NSOM cannot only be used for visualization with high lateral resolution, but also for direct writing of ferroelectric domain structures [216]. For this purpose, the instrument is used in the illumination mode (i), with an Ar^+-ion laser beam being coupled into the fiber. The sample was a cleaved TGS single crystal, and the smallest lines that could be written had a width of only 60 nm. The output light intensity at the tip was around 200 W/cm^2 (to be compared to that of direct writing by confocal microscopy techniques in $LiNbO_3$, which was realized with 10^5 W/cm^2 [29]). Although the physical mechanism behind the domain writing in TGS with such low light intensities is not yet clear – the authors in [216] propose charge removal, or photochemistry or heating through the tip – this technique is clearly very promising for future applications.

6.3 *Apertureless near-field scanning optical microscopy (ANSOM)*

Standard NSOM measurements are limited in lateral resolution by the size of the opening of the tip: the smaller the opening, the lower the light transmission and therefore the higher the noise level. This trade-off leads to a lateral resolution limit of about 50 nm [217]. However, there is a detection scheme in the near-field that overcomes this limitation: the apertureless NSOM (ANSOM). The idea is to bring a nm-sized scattering center into the near field of the surface, which can be illuminated from (i) the same side or (ii) from the back

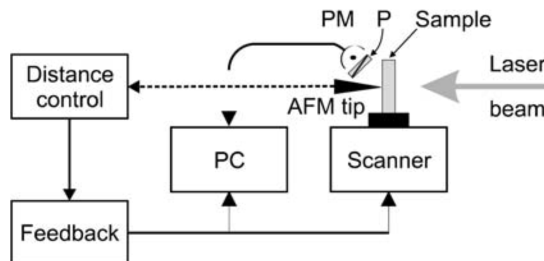

FIGURE 40 Schematic setup for ANSOM, with the sample being illuminated from the back side. A SFM tip scatters the light in the vicinity of the surface, which is detected with a photomultiplier (PM) behind an optional polarizer (P). The feedback is realized with a distance control based on SFM techniques (not explicitly drawn)

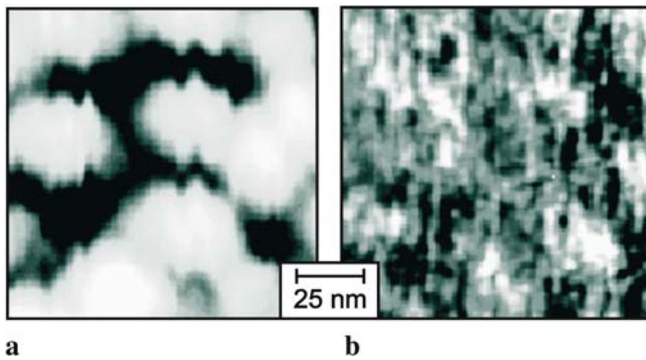

FIGURE 41 Tapping-mode AFM image (**a**) and simultaneously acquired ANSOM image (**b**). ANSOM images are distinct, exhibiting fine structure not seen in the topography. Images recorded with different applied electric fields showed a change in the ANSOM image, therefore indicating a change of the ferroelectric polarization in the film, whereas the topography was not affected (from Ref. [219])

side of the sample. The latter case is schematically depicted in Fig. 40. In its simplest setup, a standard scanning force microscope is utilized, where a laser spot is focused in the vicinity of the tip and a suitable photomultiplier records the light scattered from the tip.

Bulk TGS samples with 180° domains perpendicular to the surface were investigated with ANSOM resulting in a lateral resolution (given by the pixel size of the PC image acquisition) of only 35 nm, as determined from phase maps of the detected light [218]. The domains were revealed by applying a small modulated voltage to the tip in addition to illumination with a 633-nm HeNe laser beam. The SFM was operated in tapping mode with the resonance frequency of the cantilever being equal to that of the voltage applied. A series of experiments was carried out to ensure that the demodulated optical signal detected with the photomultiplier shows domain contrast due to the electro-optically modified birefringence and hence a change of the light polarization.

In investigations using a detection mechanism very similar to that in Ref. [220], the local surface polarization charges are measured and a lateral resolution of only 3 nm was specified, as determined from Fig. 41 [219]. This result was obtained

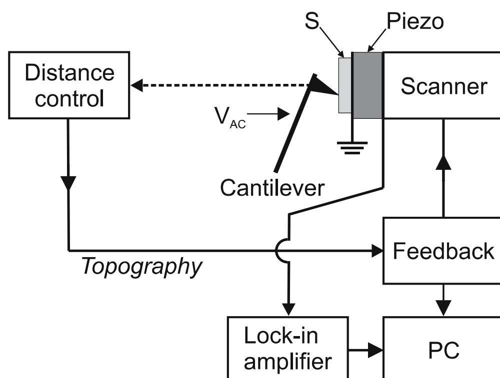

FIGURE 42 Block diagram of the scanning near-field acoustic microscope. The sample S is mounted on a piezoelectric transducer. Acoustic waves are generated in the sample via the converse piezoelectric effect through a modulated voltage applied to the tip. The acoustic waves are detected at the back side of the piezoelectric transducer as an electrical signal and analyzed with lock-in amplification

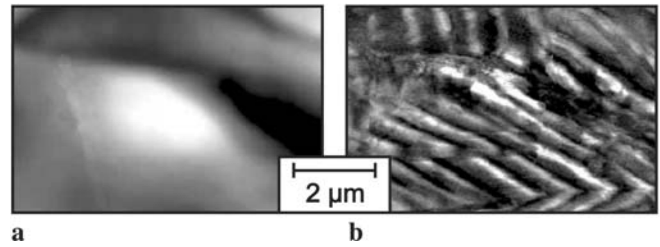

FIGURE 43 Topography (**a**) and simultaneously recorded SNAM image (**b**) revealing the domain configuration of a $BaTiO_3$ grain (from Ref. [140])

for very thin films of $Ba_xSr_{1-x}TiO_3$ ceramics. This number is even more astonishing as in other experiments, measuring hysteresis curves with piezoresponse force microscopy, it was suggested to having reached the limit of ferroelectricity in 20-nm lead titanate nanograins [4].

6.4 *Scanning near-field acoustic microscopy (SNAM)*

Scanning near-field acoustic microscopy (SNAM) [221] makes use of the converse piezoelectric effect. Applying an alternating voltage to the sample with the help of the SFM tip causes an expansion/contraction of the sample, and acoustic waves are generated. Because the sample is directly contacted to a piezoelectric transducer, this thickness change is transformed to an electrical signal via the piezoelectric effect, which can be read out with a lock-in amplifier. A schematic diagram of the setup is shown in Fig. 42. Although this technique is mostly applied to ceramics [140, 222, 223] it was also used to vizualize ferroelectric domains in PPLN [141].

The lateral resolution of this detection method, applied to ceramics, is about 50 nm (Fig. 43). Comparing SNAM measurements with DC-EFM measurements revealed identical domain structure with similar lateral resolution, therefore underlying that SNAM images ferroelectric domain properties of the samples [224].

Although the experimental setup is completely different, the principle of domain imaging is the same as in scanning electron acoustic microscopy (Sect. 5.2).

6.5 *Other scanning probe techniques*

The overview of the scanning probe techniques given above is of course not complete. Several other detection schemes for the visualization of ferroelectric domains or domain boundaries have been carried out such as scanning microwave microscopy [225], scanning resistive microscopy [226], or scanning thermal microscopy [227], to give just three more examples.

6.6 *Comparative summary: scanning probe microscopy techniques*

Although a large number of SFM techniques has been applied to the detection of ferroelectric domains, mainly the DC-EFM (contact mode with a modulated voltage applied to the tip) is utilized. This is because it can be simply adapted to standard commercial SFM, needs no special preparation of the sample, and resolves domain patterns with a lateral

resolution better than 100 nm. Is has to be pointed out that SNDM (scanning nonlinear dielectric microscopy) has shown the highest lateral resolution ($\ll 10$ nm), which might be due to the ultra-thin samples used. The setup for this detection scheme, however, is much more complicated.

7 Conclusions

Ferroelectric domain manipulation and characterization are still a challenging research area, whereas basic understanding as well as optimization of the materials for their respective applications are intensively investigated. Therefore, the visualization of domain patterns is crucial for further progress. Several techniques have been developed to satisfy the different requirements such as high lateral resolution, three-dimensional imaging, or in situ visualization. It appears that many of the methods for detection also allow the direct writing of domain patterns, by slightly changing the experimental parameters. This is extremely interesting as controlled, nm-sized structuring of ferroelectric domains becomes increasingly important for a wide range of applications.

ACKNOWLEDGEMENTS I thank K. Buse for valuable discussions and R.W. Eason and V. Gopalan for carefully reading the manuscript. Financial support from the Deutsche Telekom AG and the Deutsche Forschungsgemeinschaft (DFG research unit 557) are gratefully acknowledged.

REFERENCES

1 J. Valasek, Phys. Rev. **17**, 475 (1921)
2 G. Busch, P. Scherrer, Naturwissenschaften **23**, 737 (1935)
3 B. Matthias, A. von Hippel, Phys. Rev. **73**, 1378 (1948)
4 A. Roelofs, T. Schneller, K. Szot, R. Waser, Appl. Phys. Lett. **81**, 5231 (2002)
5 Y. Cho, K. Fujimoto, Y. Hiranaga, Y. Wagatsuma, A. Onoe, K. Terabe, K. Kitamura, Appl. Phys. Lett. **81**, 4401 (2002)
6 T. Tybell, P. Paruch, T. Giamarchi, J.-M. Triscone, Phys. Rev. Lett. **89**, 097 601 (2002)
7 T.J. Yang, V. Gopalan, P.J. Swart, U. Mohideen, Phys. Rev. Lett. **82**, 4106 (1999)
8 S. Kim, V. Gopalan, A. Gruverman, Appl. Phys. Lett. **80**, 2740 (2002)
9 M. de Angelis, S. De Nicola, A. Finizio, G. Pierattini, P. Ferraro, S. Grilli, M. Paturzo, Appl. Phys. Lett. **85**, 2785 (2004)
10 J.A. Armstrong, N. Bloembergen, J.J. Ducuing, P.S. Pershan, Phys. Rev. **127**, 1918 (1962)
11 M.M. Fejer, G.A. Magel, D.H. Jundt, R.L. Byer, IEEE J. Quantum Electron. **QE-28**, 2631 (1992)
12 M. Müller, E. Soergel, K. Buse, Appl. Phys. Lett. **83**, 1824 (2003)
13 T. Hidaka, T. Maruyama, M. Saitoh, N. Mikoshiba, M. Shimizu, T. Shiosaki, L.A. Wills, R. Hiskes, S.A. Dicarolis, J. Amano, Appl. Phys. Lett. **68**, 2358 (1996)
14 N.G.R. Broderick, G.W. Ross, H.L. Offerhaus, D.J. Richardson, D.C. Hanna, Phys. Rev. Lett. **84**, 4345 (2000)
15 R.W. Eason, A.S. Boyland, S. Mailis, P.G.R. Smith, Opt. Commun. **197**, 201 (2001)
16 R.S. Cudney, L.A. Ríos, H.M. Escamilla, Opt. Express **12**, 5783 (2004)
17 J.F. Nye (ed.), *Physical Properties of Crystals* (Oxford University Press, Oxford, 1985)
18 M.E. Lines, A.M. Glass, *Principles and Applications of Ferroelectrics and Related Materials* (Oxford University Press, New York, 2001)
19 A. Ballato, IEEE T. Ultrason. Ferr. **42**, 916 (1995)
20 M. Yamada, N. Nada, M. Saitoh, K. Watanabe, Appl. Phys. Lett. **62**, 435 (1993)
21 V.Y. Shur, E.L. Rumyantsev, E.V. Nikolaeva, E.I. Shishkin, D.V. Fursov, R.G. Batchko, L.A. Eyres, M.M. Fejer, R.L. Byer, Appl. Phys. Lett. **76**, 143 (2000)
22 S. Thaniyavarn, T. Findakly, D. Booher, J. Moen, Appl. Phys. Lett. **46**, 933 (1985)
23 A. Agronin, Y. Rosenwaks, G. Rosenman, Appl. Phys. Lett. **85**, 452 (2004)
24 G. Rosenman, P. Urenski, A. Agronin, Y. Rosenwaks, M. Molotskii, Appl. Phys. Lett. **82**, 103 (2003)
25 G. Rosenman, P. Urenski, A. Agronin, A. Arie, Y. Rosenwaks, Appl. Phys. Lett. **82**, 3934 (2003)
26 C. Restoin, C. Darraud-Taupiac, J.L. Decossas, J.C. Vareille, J. Hauden, A. Martinez, J. Appl. Phys. **88**, 6665 (2000)
27 J.-W. Son, Y. Yuen, S.S. Orlov, L. Galambos, L. Hesselink, J. Cryst. Growth **280**, 135 (2005)
28 C.L. Sones, C.E. Valdivia, J.G. Scott, S. Mailis, R.W. Eason, D.A. Scrymgeour, V. Gopalan, T. Jungk, E. Soergel, Appl. Phys. B **80**, 341 (2005)
29 A. Dierolf, C. Sandmann, Appl. Phys. Lett. **84**, 3978 (2004)
30 J. Webjörn, J. Amin, M. Hempstead, P.S. Russel, J.S. Wilkinson, Electron. Lett. **30**, 2135 (1994)
31 A.C. Busacca, C.L. Sones, R.W. Eason, S. Mailis, K. Gallo, R.T. Bratfalean, N.G. Broderick, Ferroelectrics **296**, 3 (2003)
32 T. Jungk, E. Soergel, Appl. Phys. Lett. **86**, 242 901 (2005)
33 P. Günter, J.P. Huignard (eds.), *Photorefractive Materials and Their Applications 1: Basic Effects* (Springer Ser. Opt. Sci. **113**) (Springer, Berlin, 2005)
34 V. Gopalan, T.E. Mitchell, J. Appl. Phys. **85**, 2304 (1999)
35 D.A. Scrymgeour, V. Gopalan, A. Itagi, A. Saxena, P.J. Swart, Phys. Rev. B **71**, 184 110 (2005)
36 T. Volk, D. Isakov, N. Ivanov, L. Ivleva, K. Betzler, A. Tunyagi, M. Wöhlecke, J. Appl. Phys. **97**, 074 102 (2005)
37 A.M. Glass, J. Appl. Phys. **40**, 4699 (1969)
38 F. Micheron, C. Mayeux, J.C. Trotier, Appl. Opt. **13**, 784 (1974)
39 A.S. Kewitsch, T.W. Towe, G.J. Salamo, A. Yariv, M. Zhang, M. Segev, E.J. Sharp, R.R. Neurgaonkar, Appl. Phys. Lett. **66**, 1865 (1995)
40 T. Ozaki, K. Fujii, S. Aoyagi, J. Appl. Phys. **80**, 1697 (1996)
41 D. Shur, G. Rosenman, Y.E. Krasik, Appl. Phys. Lett. **70**, 574 (1997)
42 A.N. Holden, B.T. Matthias, W.J. Merz, J.P. Remeika, Phys. Rev. **98**, 546 (1955)
43 B.J.B. Schein, E.C. Lingafelter, J.M. Stewart, J. Chem. Phys. **47**, 5183 (1967)
44 A.N. Holden, W.J. Merz, J.P. Remeika, B.T. Matthias, Phys. Rev. **101**, 962 (1956)
45 O. Kolosov, A. Gruverman, J. Hatano, K. Takahashi, H. Tokumoto, Phys. Rev. Lett. **74**, 4309 (1995)
46 A. Gruverman, O. Kolosov, J. Hatano, K. Takahashi, H. Tokumoto, J. Vac. Sci. Technol. B **13**, 1095 (1995)
47 R.S. Weis, T.K. Gaylord, Appl. Phys. A **37**, 191 (1985)
48 R.T. Smith, F.S. Welsh, J. Appl. Phys. **42**, 2219 (1971)
49 H. Ogi, Y. Kawasaki, M. Hirao, H. Ledbetter, J. Appl. Phys. **92**, 2451 (2002)
50 K. Kitamura, Y. Furukawa, K. Niwa, V. Gopalan, T.E. Mitchell, Appl. Phys. Lett. **73**, 3073 (1998)
51 D. Berlincourt, H. Jaffe, Phys. Rev. **111**, 143 (1958)
52 M. Zgonik, P. Bernasconi, M. Duelli, R. Schlesser, P. Günter, M.H. Garrett, D. Rytz, Y. Zhu, X. Wu, Phys. Rev. B **50**, 5941 (1994)
53 S. Ducharme, J. Feinberg, R.R. Neurgaonkar, IEEE J. Quantum Electron. **QE-23**, 2116 (1987)
54 Y. Wang, W. Kleemann, T. Woike, R. Pankrath, Phys. Rev. B **61**, 3333 (2000)
55 G. Rosenman, A. Skliar, M. Oron, M. Katz, J. Phys. D **30**, 277 (1997)
56 N. Angert, M. Tseitlin, E. Yashchin, M. Roth, Appl. Phys. Lett **67**, 1941 (1995)
57 H. Graafsma, G.W.J.C. Heunen, S. Dahaoui, A.E. Haouzi, N.K. Hansen, G. Marnier, Acta Crystallogr. B **53**, 565 (1997)
58 R.C. Eckardt, H. Masuda, Y.X. Fan, R.L. Byer, IEEE J. Quantum Electron. **QE-26**, 922 (1990)
59 W.P. Mason, Phys. Rev. **69**, 173 (1946)
60 K. Takizawa, M. Okada, J. Opt. Soc. Am. B **2**, 289 (1985)
61 J.W. Hong, K.H. Noh, S. Park, S.I. Kwun, Z.G. Kim, Phys. Rev. B **58**, 5078 (1998)
62 R. Lüthi, H. Haefke, K.P. Meyer, E. Meyer, L. Howald, H.J. Guntherodt, J. Appl. Phys. **74**, 7461 (1993)
63 S.V. Kalinin, D.A. Bonnell, Phys. Rev. B **63**, 125 411 (2001)
64 S.V. Kalinin, D.A. Bonnell, Nano Lett. **4**, 555 (2004)
65 G.L. Pearson, W.L. Feldmann, J. Phys. Chem. Solids **9**, 28 (1959)
66 J. Hatano, F. Suda, H. Futama, Jpn. J. Appl. Phys. **12**, 1644 (1973)

67 Y. Furuhata, K. Toriyama, Appl. Phys. Lett. **23**, 361 (1973)
68 N.A. Tikhomirova, S.A. Pikinand, L.A. Shuvalov, L.I. Dontsova, E.S. Popov, A.V. Shilnikov, L.G. Bulatova, Ferroelectrics **29**, 145 (1980)
69 N.R. Ivanov, N.A. Tikhomirova, A.V. Ginzberg, S.P. Chumakova, S.M. Osadchij, E.Y. Nikiruj, Ferroelectr. Lett. **15**, 127 (1993)
70 M. Qi, N.A. Tikhomirova, L.A. Shuvalov, J. Appl. Phys. **79**, 3188 (1996)
71 J.F. Blach, R. Desfeux, A. Da Costa, D. Bormann, J.F. Henninot, M. Warenghem, W. Prellier, Liq. Cryst. **31**, 1241 (2004)
72 J. Fousek, M. Safránková, J. Kaczér, Appl. Phys. Lett. **8**, 192 (1966)
73 J.A. Hooton, W.J. Merz, Phys. Rev. **98**, 409 (1955)
74 H.L. Stadler, P.J. Zachmanidis, J. Appl. Phys. **34**, 3255 (1963)
75 R.C. Miller, A. Savage, Phys. Rev. Lett. **2**, 294 (1959)
76 H.L. Stadler, J. Appl. Phys. **34**, 570 (1963)
77 H. Nassau, H.J. Levinstein, G.M. Loiacono, Appl. Phys. Lett. **6**, 228 (1965)
78 W.L. Holstein, J. Cryst. Growth **171**, 477 (1996)
79 Y. Zheng, E. Shi, S. Wang, Z. Lu, S. Cui, L. Wang, W. Zhong, Cryst. Res. Technol. **39**, 387 (2004)
80 I.E. Barry, G.W. Ross, P.G.R. Smith, R.W. Eason, Appl. Phys. Lett. **74**, 1487 (1999)
81 C. Sones, S. Mailis, V. Apostolopoulos, I.E. Barry, C. Gawith, P.G.R. Smith, R.W. Eason, J. Micromech. Microeng. **12**, 53 (2002)
82 D. Xue, K. Kitamura, Ferroelectr. Lett. **29**, 89 (2002)
83 M. Müller, E. Soergel, M.C. Wengler, K. Buse, Appl. Phys. B **78**, 367 (2004)
84 X. Liu, K. Terabe, M. Nakamura, S. Takekawa, K. Kitamura, J. Appl. Phys. **97**, 064 308 (2005)
85 Y. Hiranaga, Y. Wagatsuma, Y. Cho, Jpn. J. Appl. Phys. **43**, L569 (2004)
86 A.S. Kewitsch, A. Saito, A. Yariv, M. Segev, R.R. Neurgaonkar, J. Opt. Soc. Am. B **12**, 1460 (1995)
87 Z.W. Hu, P.A. Thomas, P.Q. Huang, Phys. Rev. B **56**, 8559 (1997)
88 A. Sawada, R. Abe, Jpn. J. Appl. Phys. **6**, 677 (1967)
89 N. Nakatani, Jpn. J. Appl. Phys. **25**, 27 (1986)
90 A.R. Patel, C.C. Desai, J. Appl. Crystallogr. **2**, 268 (1972)
91 V. Bermúdez, F. Caccavale, C. Sada, F. Segato, E. Diéguez, J. Cryst. Growth **191**, 589 (1998)
92 H.W. Chong, A. Mitchell, M.W. Austin, Wet etching techniques for the realisation of novel electrode structures on X and Z-cut lithium niobate. COMMAND 2000 Proceedings, Conference on Optoelectronic and Microelectronic Materials and Devices (Cat. No. 00EX466), Bundoora, Vic., Australia, 6–8 December 2000, ed. by L.D. Broekman, B.F. Usher, J.D. Riley, IEEE, Pisacataway, NJ, USA (2000) p 194-7 of x+554 pages, 8 refs. Also available on CD-ROM in PDF format
93 I.E. Barry, G.W. Ross, P.G.R. Smith, R.W. Eason, G. Cook, Mater. Lett. **37**, 246 (1998)
94 S. Mailis, G.W. Ross, L. Reekie, J.A. Abernethy, R.W. Eason, Electron. Lett. **36**, 1801 (2000)
95 J. Capmany, C.R. Fernández-Pousa, E. Diéguez, V. Bermúdez, Appl. Phys. Lett. **83**, 5145 (2003)
96 W.J. Merz, Phys. Rev. **88**, 421 (1952)
97 V. Gopalan, T.E. Mitchell, Y. Furukawa, K. Kitamura, Appl. Phys. Lett. **72**, 1981 (1998)
98 S. Chao, W. Davis, D.D. Tuschel, R. Nichols, M. Gupta, H.C. Cheng, Appl. Phys. Lett. **67**, 1066 (1995)
99 B. Zwicker, P. Scherrer, Helv. Phys. Acta **17**, 346 (1944)
100 H.F. Kay, Acta Crystallogr. **1**, 229 (1948)
101 W.J. Merz, Phys. Rev. **95**, 690 (1954)
102 G.K.H. Pang, K.Z. Baba-Kishi, J. Phys. D **31**, 2846 (1998)
103 V. Gopalan, S.S.A. Gerstl, A. Itagi, T.E. Mitchell, Q.X. Jia, T.E. Schlesinger, D.D. Stancil, J. Appl. Phys. **86**, 1638 (1999)
104 M. Müller, E. Soergel, K. Buse, Opt. Lett. **28**, 2515 (2003)
105 M. Müller, E. Soergel, K. Buse, C. Langrock, M.M. Fejer, J. Appl. Phys. **97**, 044 102 (2005)
106 M. Müller, E. Soergel, K. Buse, Appl. Opt. **43**, 6344 (2004)
107 M.C. Wengler, Ph.D. thesis, University of Bonn (2005)
108 B. Sugg, F. Kahmann, R. Pankrath, R.A. Rupp, Appl. Opt. **33**, 5386 (1994)
109 P. Günter, J.P. Huignard (eds.), *Photorefractive Materials and Their Applications I* (Top. Appl. Phys. **61**) (Springer, Berlin, 1988)
110 P. Günter, J.P. Huignard (eds.), *Photorefractive Materials and Their Applications II* (Top. Appl. Phys. **62**) (Springer, Berlin, 1989)
111 K. Buse, Appl. Phys. B **64**, 273 (1997)
112 K. Buse, Appl. Phys. B **64**, 391 (1997)
113 S. MacCormack, J. Feinberg, Appl. Opt. **35**, 5961 (1996)
114 V. Grubsky, S. MacCormack, J. Feinberg, Opt. Lett. **21**, 6 (1996)
115 G. Dolino, Appl. Phys. Lett. **22**, 123 (1973)
116 S. Kurimura, Y. Uesu, J. Appl. Phys. **81**, 369 (1997)
117 Y. Uesu, S. Kurimura, Y. Yamamoto, Appl. Phys. Lett. **66**, 2165 (1995)
118 S.I. Bozhevolnyi, J.M. Hvam, K. Pedersen, F. Laurell, H. Karlsson, T. Skettrup, M. Belmonte, Appl. Phys. Lett. **73**, 1814 (1998)
119 A.I. Otko, A.E. Nosenko, V.N. Moiseenko, Crystallogr. Rep. **39**, 444 (1994)
120 R.J. Gehr, W.J. Alford, A.V. Smith, Appl. Opt. **37**, 3311 (1998)
121 M. Flörsheimer, R. Paschotta, U. Kubitscheck, C. Brillert, D. Hofmann, L. Heuer, G. Schreiber, C. Verbeek, W. Sohler, H. Fuchs, Appl. Phys. B **67**, 593 (1998)
122 I.I. Smolyaninov, A.V. Zayats, C.C. Davis, Opt. Lett. **22**, 1592 (1997)
123 M. Canut, R. Hosemann, Acta Crystallogr. **17**, 973 (1964)
124 G. Fogarty, B. Steiner, M. Cronin-Golomb, U. Laor, M.H. Garrett, J. Martin, R. Uhrin, J. Opt. Soc. Am. B **13**, 2636 (1996)
125 B.W. Batterman, H. Cole, Rev. Mod. Phys. **36**, 681 (1964)
126 Z.W. Hu, P.A. Thomas, A. Snigirev, I. Snigireva, A. Souvorov, P.G.R. Smith, G.W. Ross, S. Teat, Nature **392**, 690 (1998)
127 P. Rejmánková-Pernot, P. Cloetens, J. Baruchel, J.-P. Guigay, P. Moretti, Phys. Rev. Lett. **81**, 3435 (1998)
128 P. Pernot-Rejmánková, P.A. Thomas, P. Cloetens, F. Lorut, J. Baruchel, Z.W. Hu, P. Urenski, G. Rosenman, J. Appl. Crystallogr. **33**, 1149 (2000)
129 Z.W. Hu, P.A. Thomas, W.P. Risk, Phys. Rev. B **59**, 14 259 (1999)
130 S. Kim, V. Gopalan, B. Steiner, Appl. Phys. Lett. **77**, 2051 (2000)
131 T. Jach, S. Kim, V. Gopalan, S. Durbin, D. Bright, Phys. Rev. B **69**, 064 113 (2004)
132 R.C. Rogan, N. Tamura, G.A. Swift, E. Üstündag, Nat. Mater. **2**, 379 (2003)
133 R. Le Bihan, Ferroelectrics **97**, 19 (1989)
134 A.A. Sogr, Ferroelectrics **97**, 47 (1989)
135 S. Zhu, W. Cao, Phys. Status Solidi A **173**, 495 (1999)
136 G. Rosenman, A. Skliar, Y. Lareah, N. Angert, M. Tseitlin, M. Roth, M. Oron, M. Katz, J. Appl. Phys. **80**, 7166 (1996)
137 W. Cao, Microsc. Microanal. **10**, 1072 (2004)
138 S. Zhu, W. Cao, Phys. Rev. Lett. **79**, 2558 (1997)
139 B.Y. Zhang, F.M. Jiang, Q.R. Ying, S. Kojima, J. Appl. Phys. **80**, 1916 (1996)
140 X.X. Liu, R. Heiderhoff, H.P. Abicht, L.J. Balk, J. Phys. D **35**, 74 (2002)
141 F. Augereau, G. Despaux, P. Saint-Grégoire, Ferroelectrics **290**, 29 (2003)
142 T. Malis, H. Gleiter, J. Appl. Phys. **47**, 5195 (1976)
143 M.A. Zurbuchen, G. Asayama, D.G. Schlom, S.K. Streiffer, Phys. Rev. Lett. **88**, 107 601 (2002)
144 Y. Ding, J.S. Liu, Y.N. Wang, Appl. Phys. Lett. **76**, 103 (2000)
145 S.B. Ren, C.J. Lu, J.S. Liu, H.M. Shen, Y.N. Wang, Phys. Rev. B **54**, 14 337 (1996)
146 Y.L. Li, L.Q. Chen, G. Asayama, D.G. Schlom, M.A. Zurbuchen, S.K. Streiffer, J. Appl. Phys. **95**, 6332 (2004)
147 D.J. You, W.W. Jung, S.K. Choi, Y. Cho, Appl. Phys. Lett. **84**, 3346 (2004)
148 Y.H. Hu, H.M. Chan, X.W. Zhang, M.P. Harmer, J. Am. Ceram. Soc. **69**, 594 (1986)
149 N. Floquet, C.M. Valot, M.T. Mesnier, J.C. Niepce, L. Normand, A. Thorel, R. Kilaas, J. Phys. III **7**, 1105 (1997)
150 S. Stemmer, S.K. Streiffer, F. Ernst, M. Ruehle, Philos. Mag. A **713**, 713 (1995)
151 M. Foeth, A. Sfera, P. Stadelmann, P.-A. Buffat, J. Electron Microsc. **48**, 717 (1999)
152 M. Foeth, P. Stadelmann, P.-A. Buffat, Ultramicroscopy **75**, 203 (1999)
153 X. Zhang, T. Hashimoto, D.C. Joy, Appl. Phys. Lett. **60**, 784 (1992)
154 D. Gabor, Proc. R. Soc. Lon. Ser.-A **197**, 454 (1949)
155 H. Lichte, M. Reibold, K. Brand, M. Lehmann, Ultramicroscopy **93**, 199 (2002)
156 R.H. Webb, Rep. Prog. Phys. **59**, 427 (1996)
157 C. Hubert, J. Levy, A.C. Carter, W. Chang, S.W. Kiechoefer, J.S. Horwitz, D.B. Chrisey, Appl. Phys. Lett. **71**, 3353 (1997)
158 O. Tikhomirov, B. Red'kin, A. Trivelli, J. Levy, J. Appl. Phys. **87**, 1932 (2000)
159 C. Hubert, J. Levy, E. Cukauskas, Phys. Rev. Lett. **85**, 1998 (2000)
160 A. Rosenfeldt, M. Flörsheimer, Appl. Phys. B **73**, 523 (2001)

161 V. Dierolf, M. Koerdt, Phys. Rev. B **61**, 8043 (2000)
162 V. Dierolf, C. Sandmann, S. Kim, V. Gopalan, K. Polgar, J. Appl. Phys. **93**, 2295 (2003)
163 The image published in Ref. [162] is a little diferent because of a misprint (private communication from V. Dierolf)
164 G. Binning, C.F. Quate, C. Gerber, Phys. Rev. Lett. **56**, 930 (1986)
165 F. Saurenbach, B.D. Terris, Appl. Phys. Lett. **56**, 1703 (1990)
166 M. Labardi, V. Likodimos, M. Allegrini, Phys. Rev. B **61**, 14 390 (2000)
167 S. Hong, J. Woo, H. Shin, J.U. Jeon, Y.E. Pak, E.L. Colla, N. Setter, E. Kim, K. No, J. Appl. Phys. **89**, 1377 (2001)
168 M. Alexe, A. Gruverman (eds.), *Nanoscale Characterisation of Ferroelectric Materials*, 1st edn. (Springer, Berlin New York, 2004)
169 S.V. Kalinin, D.A. Bonnell, Phys. Rev. B **65**, 125 408 (2002)
170 C. Harnagea, A. Pignolet, M. Alexe, D. Hesse, Integr. Ferroelectr. **44**, 113 (2002)
171 L.M. Eng, H.J. Güntherodt, G. Rosenman, A. Skliar, M. Oron, M. Katz, D. Eger, J. Appl. Phys. **83**, 5973 (1998)
172 D.A. Scrymgeour, V. Gopalan, Phys. Rev. B **72**, 024 103 (2005)
173 J.W. Hong, D.S. Kahng, J.C. Shin, H.J. Kim, Z.G. Khim, J. Vac. Sci. Technol. B **16**, 2942 (1998)
174 J.W. Hong, S. Park, Z.G. Khim, Rev. Sci. Instrum. **70**, 1735 (1999)
175 M. Shvebelman, P. Urenski, R. Shikler, G. Rosenman, Y. Rosenwaks, M. Molotskii, Appl. Phys. Lett. **80**, 1806 (2002)
176 D. Sarid, *Scanning Force Microscopy*, revised edn. (Oxford University Press, New York, 1994)
177 E. Meyer, H.J. Hug, R. Bennewitz, *Scanning Probe Microscopy: The Lab on a Tip*, 1st edn. (Springer, Berlin New York, 2003)
178 TappingMode and LiftMode are registered trademarks of Digital Instruments Inc., U.S. Patents 5,266,801 and 5,308,974
179 S. Hong, H. Shin, J. Woo, K. No, Appl. Phys. Lett. **80**, 1453 (2002)
180 F.J. Giessibl, S. Hembacher, H. Bielefeldt, J. Mannhart, Science **289**, 422 (2000)
181 R. Lüthi, H. Haefke, W. Gutmannsbauer, E. Meyer, L. Howald, H.-J. Güntherodt, J. Vac. Sci. Technol. B **12**, 2451 (1994)
182 H. Bluhm, U.D. Schwarz, R. Wiesendanger, Phys. Rev. B **57**, 161 (1998)
183 L.M. Eng, M. Friedrich, J. Fousek, P. Günter, J. Vac. Sci. Technol. B **14**, 1191 (1996)
184 T. Jungk, E. Soergel, Appl. Phys. Lett. **86**, 202 901 (2005)
185 Y. Rosenwaks, M. Molotskii, A. Agronin, P. Urenski, M. Shvebelman, G. Rosenman, Nanodomain engineering in ferroelectric crystals using high voltage atomic force microscopy, in *Nanoscale Characterisation of Ferroelectric Materials*, 1st edn. (Springer, Berlin New York, 2004), pp. 221–265
186 H.-N. Lin, S.-H. Chen, S.-T. Ho, P.-R. Chen, I.-N. Lin, J. Vac. Sci. Technol. B **21**, 916 (2003)
187 B.J. Rodriguez, R.J. Nemanich, A. Kingon, A. Gruverman, S.V. Kalinin, K. Terabe, X.Y. Liu, K. Kitamura, Appl. Phys. Lett. **86**, 012 906 (2005)
188 B.J. Rodriguez, A. Gruverman, A.I. Kingon, R.J. Nemanich, O. Ambacher, Appl. Phys. Lett. **80**, 4166 (2002)
189 J.W. Burgess, J. Phys. D **8**, 283 (1975)
190 M. Labardi, V. Likodimos, M. Allegrini, Appl. Phys. A **72**, S79 (2001)
191 C. Harnagea, A. Pignolet, M. Alexe, D. Hesse, Integr. Ferroelectr. **60**, 101 (2004)
192 T. Jungk, A. Hoffmann, E. Soergel, to be published
193 G. Hu, T. Tang, J. Xu, J. Appl. Phys. **41**, 6793 (2002)
194 S.V. Kalinin, D.A. Bonnell, J. Mater. Res. **17**, 936 (2002)
195 S.V. Kalinin, E. Karapetian, M. Kachanov, Phys. Rev. B **70**, 184 101 (2004)
196 V. Bermúdez, A. Gil, L. Arizmendi, J. Colchero, A.M. Baró, E. Diéguez, J. Mater. Res. **15**, 2814 (2000)
197 Y. Cho, A. Kirihara, T. Saeki, Rev. Sci. Instrum. **67**, 2297 (1996)
198 C. Gao, F. Duewer, Y. Lu, X.-D. Xiang, Appl. Phys. Lett. **73**, 1146 (1998)
199 H. Odagawa, Y. Cho, Jpn. J. Appl. Phys. **39**, 5719 (2000)
200 Y. Cho, S. Kazuta, K. Matsuura, Appl. Phys. Lett. **75**, 2833 (1999)
201 T. Morita, Y. Cho, Appl. Phys. Lett. **84**, 257 (2004)
202 J.E. Stern, B.D. Terris, H.J. Mamin, D. Rugar, Appl. Phys. Lett. **53**, 2717 (1988)
203 Y. Martin, D.W. Abraham, H. Wickramasinghe, Appl. Phys. Lett. **52**, 1103 (1987)
204 C. Schoeneberger, S.F. Alvarado, Phys. Rev. Lett. **65**, 3162 (1990)
205 E. Soergel, R. Pankrath, K. Buse, Ferroelectrics **296**, 19 (2003)
206 P. Lehnen, J. Dec, W. Kleemann, J. Phys. D **33**, 1932 (2000)
207 K.L. Babcock, V.B. Elings, J. Shi, D.D. Awschalom, M. Dugas, Appl. Phys. Lett. **69**, 705 (1996)
208 H. Bluhm, A. Wadas, R. Wiesendanger, A. Roshko, J.A. Aust, D. Nam, Appl. Phys. Lett. **71**, 146 (1997)
209 H. Bluhm, A. Wadas, R. Wiesendanger, K.P. Meyer, L. Szcześniak, Phys. Rev. B **55**, 4 (1997)
210 D.W. Pohl, W. Denk, M. Lanz, Appl. Phys. Lett. **44**, 651 (1984)
211 E. Betzig, J.K. Trautman, Science **257**, 189 (1992)
212 E. Betzig, J.K. Trautman, T.D. Harris, J.S. Weiner, Science **251**, 1468 (1991)
213 T.J. Yang, U. Mohideen, M.C. Gupta, Appl. Phys. Lett. **71**, 1960 (1997)
214 T.J. Yang, U. Mohideen, Phys. Lett. A **250**, 205 (1998)
215 S. Kim, V. Gopalan, Mater. Sci. Eng. B **120**, 91 (2005)
216 J. Massanell, N. Garcia, A. Zlatkin, Opt. Lett. **21**, 12 (1996)
217 D. Courjon (ed.), *Near Field Microscopy and Near Field Optics*, 1st edn. (Imperial College Press, London, 2003)
218 X.K. Orlik, M. Labardi, M. Allegrini, Appl. Phys. Lett. **77**, 2042 (2000)
219 C. Hubert, J. Levy, Appl. Phys. Lett. **73**, 3229 (1998)
220 F. Zenhausern, M.P. O'Boyle, H.K. Wickramasinghe, Appl. Phys. Lett. **65**, 1632 (1994)
221 P. Güthner, U.C. Fischer, K. Dransfeld, Appl. Phys. B **48**, 89 (1989)
222 X.X. Liu, H.P. Abicht, L.J. Balk, Ferroelectrics **274**, 285 (2002)
223 X.X. Liu, R. Heiderhoff, H.P. Abicht, L.J. Balk, Mater. Chem. Phys. **75**, 125 (2002)
224 X.X. Liu, R. Heiderhoff, H.P. Abicht, L.J. Balk, Anal. Sci. **17**, s57 (2001)
225 Y. Lu, T. Wei, F. Duewer, Y. Lu, N.-B. Ming, P.G. Schultz, X.-D. Xiang, Science **276**, 2004 (1997)
226 H. Park, J. Jung, D.-K. Min, S. Kim, S. Hong, H. Shin, Appl. Phys. Lett. **84**, 1734 (2004)
227 A. Majumdar, Annu. Rev. Mater. Sci. **29**, 505 (1999)